# A Search for Long-Lived Neutral Particles Decaying to Dijets with the CMS detector at the Large Hadron Collider

Andrzej Maciej Żurański

A Dissertation

Presented to the Faculty

of Princeton University

in Candidacy for the Degree

of Doctor of Philosophy

Recommended for Acceptance

by the Department of

Physics

Advisor: Daniel Marlow

April, 2014

# Abstract

A search is performed for long-lived massive neutral particles decaying to quark-antiquark pairs. The experimental signature is a distinctive topology of a pair of hadronic jets originating at a secondary vertex. Events were collected by the CMS detector at the LHC during pp collisions at $\sqrt{s} = 8$ TeV, and selected from data samples corresponding to 18.5 fb$^{-1}$ of integrated luminosity. No significant excess is observed above Standard Model expectations and an upper limit is set with 95% confidence level on the production cross section of a heavy scalar particle, $H^0$, in the mass range 200 to 1000 GeV, decaying into a pair of long-lived neutral $X^0$ particles in the mass range 50 to 350 GeV, where each of the $X^0$ particles decay to quark-antiquark pairs. For $X^0$ mean proper lifetimes of 0.1 to 200 cm, the upper limits are typically 0.5$-$200 fb.

# Acknowledgements

First, I would like to express deep gratitude to my principal advisor Dan Marlow. His patience, wisdom, and guidance combined with good manners have been invaluable. I am also indebted to Jim Olsen who introduced me to high energy physics and clarified the workings of physics analysis.

This dissertation has been completed in a pleasant and humane environment. This is mainly thanks to my collaborators, the long-lived group conveners Loic Quertenmont, Daniele del Re, John Paul Chou and Steve Worm, as well as the people with whom I could discuss the very details of the analysis strategy, Dan Marlow, Ian Tomalin, Emyr Clement and Paul Lujan.

I learned more than I can recall from conversations, help, and support of other fellow physics students and postdocs. I would like to specially thank Edward Laird who introduced me to python and fixed gear bicycles. I cannot omit my fellow roommate Halil Saka, he has always been a good companion, willing to discuss the physics issues or relax with the help of his inexhaustible movie collection. There is too many to name, but I would also like to thank Michael Mooney, Adam Hunt, Edmund Berry, Xiaohang Quan, Jeroen Hegeman, Paul Lujan, Seth Zenz, Rafal Staszewski, Maciej Trzebiński and Agnieszka Dziurda.

In a broad perspective I am particularly grateful to my parents, Janka and Marek, for their tremendous effort in my upbringing and education. Thanks to them I've been exposed to science and nature for as long as I can remember. Some of their explanations of the physical phenomena that I remember from childhood, i.e. the reflections from mirrors, the relativity principle, the Doppler effect etc. are still the best explanations I can find for

them.

Last but not least, I would like to thank all the other people with whom I have shared this five years for making it an exciting endeavour, in particular Marie-Luise Menzel and Agata Witek who continuously encouraged me to explore life outside of physics.

# Contents

# List of Figures

# List of Tables

# Chapter 1

# Introduction

The Standard Model is the theoretical framework that describes fundamental particles and their interactions. It explains a wealth of results from accelerator-based and cosmic ray-based experiments, with great accuracy in most cases. The recent discovery of a Higgs boson, which is a long sought particle thought to be responsible for electroweak symmetry breaking, emphasizes the success of the theory.

Nevertheless, significant pieces of the Standard Model are still obscure: the hierarchy problem, the unification of the fundamental forces at very small distances and their possible connection to gravity, the dark matter and dark energy hypotheses, etc. We therefore hope to observe and understand the way in which the Standard Model breaks down. The phenomena we have encountered, at the energy scales explored so far, already hint at some grander underlying structure of nature. This structure is yet to be found.

The physics goals of the experiments at the Large Hadron Collider (LHC) are to examine the internal consistency of the Standard Model while looking for its extensions. Currently, the major tasks are to explore the Standard Model Higgs sector, fully investigate the TeV mass scale with searches for new particles, and to seek connections between the particles produced in proton-proton collisions and dark matter. Described in this dissertation is a particular course of exploration: a search for hypothetical particles that haven't been observed so far. Our aim is to probe the existence of particles that are neutral, massive

and decay with a relatively long lifetime, between pico and nanoseconds. The existence of such long-lived exotic particles would offer a clue about physics that may lie beyond the Standard Model.

The thesis is structured as follows. Chapter 1 presents the Standard Model together with its open questions, it is then followed by an introduction of the Hidden Valley Standard Model extensions and the motivations for long-lived particles searches. Chapter 2 describes the LHC and the Compact Muon Solenoid (CMS) apparatus. The basic aspects of CMS event reconstruction and simulation are also explained. In Chapter 3, the details of long-lived particle reconstruction and selection are described. Chapter 4 is dedicated to the estimation of the Standard Model background, while Chapter 5 details the various sources of systematic uncertainty in the analysis. Finally, in Chapter 6, the results of the search are presented, and limits on the various signals are set.

The search has been constructed to follow a *blind analysis* approach. In such an analysis all the details of event reconstruction and selection are established with the use of simulations and control samples before the analysis of the final dataset is performed.

Natural units, in which $\hbar = c = 1$, are used throughout this thesis.

## 1.1 The Standard Model

The Standard Model is a quantum field theory of elementary particles that describes three of the four fundamental interactions: the electromagnetic, the weak, and the strong interactions. A fourth fundamental interaction, gravity, is not a part of the model as no quantum theory of gravity exists to date. The Standard Model is described in detail elsewhere, e.g. [1, 2, 3], but a brief overview is given here. From this point forward the Standard Model will be denoted as SM.

In the SM each particle is described in terms of a dynamical field that permeates space-time, while the internal dynamics and kinematics are controlled by a relativistically invariant Lagrangian. The SM is defined by the three local gauge symmetries of the Lagrangian corresponding to three fundamental interactions. Particle mass and electric charge, which are

well known properties from classical physics, are highly non-obvious quantities in the SM. They will be re-introduced together with the mechanism of electroweak symmetry breaking. At this point, however, all elementary particles are assumed to be massless and only the possible quantum numbers and degrees of freedom of particle states are investigated.

The existence of an interaction is reflected in the quantum numbers of the elementary particles, while an interaction itself can be viewed as a transformation between particle states in a manner similar to a rotation, but within an internal space of the interaction. The SM Lagrangian is assumed to be invariant under the following symmetry group:

$$\mathrm{SU(3)_C} \times \mathrm{SU(2)_L} \times \mathrm{U(1)_Y} \tag{1.1}$$

where C denotes the color interaction, L the weak isospin interaction that acts only on the left-handed part of the spinors, and Y is the hypercharge interaction.

The smallest non-trivial representation of the weak isospin interaction is a two-component doublet of particles with three generators of rotations in the isospin space denoted as $W^i$ and $i = 1, 2, 3$. Therefore, there is an "up" and a "down" type in each weak isospin doublet of elementary particles. Both quarks and leptons are arranged into doublets of weak isospin, the up quarks ($u$, $c$, $t$) are matched to down quarks ($d$, $s$, $b$), and the leptons ($e$, $\mu$, $\tau$) are matched to neutrinos ($\nu_e$, $\nu_\mu$, $\nu_\tau$). The weak isospin doublets of quarks and leptons are presented in Fig. 1.1. The hypercharge $Y$ is very similar to electric charge, although the charge assignments are such as to preserve indistinguishability of the components of weak isospin doublets.

The sub-symmetry $\mathrm{SU(2)_L} \times \mathrm{U(1)_Y}$ describes the electroweak sector of the SM with the following Lagrangian:

$$\mathcal{L}_{\mathrm{EW}} = \sum_{\psi} \bar{\psi}\gamma^{\mu} \left( i\partial_{\mu} - g' \frac{1}{2} Y B_{\mu} - g \frac{1}{2} \vec{\tau}_{\mathrm{L}} \vec{W}_{\mu} \right) \psi \tag{1.2}$$

where $B_\mu$ is the U(1) gauge field; $Y$ is the hypercharge, the generator of the U(1) group; $\vec{W}_\mu$ is the three-component SU(2) gauge field; $\vec{\tau}_{\mathrm{L}}$ are the Pauli matrices, infinitesimal generators of the SU(2) group. The subscript $L$ indicates that they only act on left-handed fermions; $g'$ and $g$ are coupling constants.

The gauge symmetry associated with the color (strong) interaction is a three-dimensional special unitary transformation SU(3). The internal space of the strong interaction has a smallest non-trivial representation given by a triplet of states, denoted as colors: red, blue, and green, and a set of eight generators of rotation. Such a color triplet is called a quark, with the three color states being indistinguishable, while the eight carriers of the strong interaction are called gluons. The quantum chromodynamics (QCD) part of the SM is described by the following Lagrangian:

$$\mathcal{L}_{QCD} = i\overline{U}(\partial_\mu - ig_s G^a_\mu T^a)\gamma^\mu U + i\overline{D}(\partial_\mu - ig_s G^a_\mu T^a)\gamma^\mu D. \tag{1.3}$$

where $G^a_\mu$ is the SU(3) gauge field containing the gluons, $\gamma^\mu$ are the Dirac matrices, D and U are the Dirac spinors associated with up- and down-type quarks, and $g_s$ is the strong coupling constant.

An interesting feature of the strong interaction is that as the energy scale of the interaction increases (the length scale decreases) the strength of the coupling constant becomes small. This phenomenon, also known as *asymptotic freedom*, is an outcome of the interaction dimension ($N = 3$) and the number of existing quark flavors (6 known flavors). Another aspect of the strong interaction is *color confinement*. Although this phenomenon is not yet well explained, it is thought to be related to the fact that gluons also carry color charge and can interact with themselves. As a result of the confinement, the color particles cannot be isolated or directly measured. The particles that carry color clump together to form groups of particles that are color neutral, which we know as the hadrons.

The particles within each of the weak isodoublets differ in terms of their mass and electric charge, making them distinguishable. Therefore the weak isospin interaction is not an observed symmetry of nature, but it was clearly present in some form given the structure of the particles table. In order to explain the physically observed masses and charges of elementary particles we need to introduce electroweak symmetry breaking, a central concept of the SM that transforms the weak isospin and hypercharge interactions into the well known weak and electromagnetic forces.

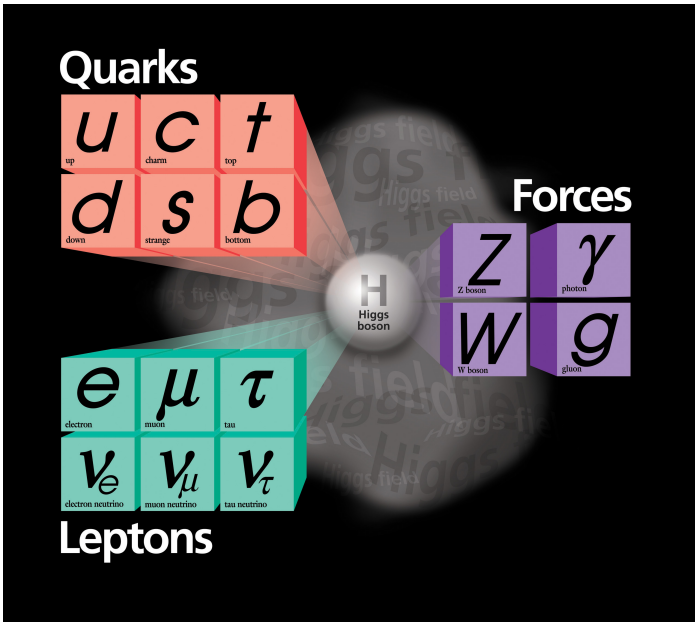


Figure 1.1: Table of elementary particles: quarks and leptons (spin-1/2) are shown on the left, the gauge bosons (spin-1) on the right, in the center the Higgs boson (spin-0).

### 1.1.1 The Higgs Mechanism

What happens if a particle field takes on a non-zero expectation value in vacuum? Depending on the quantum numbers of this non-zero field, the vacuum will not necessarily be invariant under all symmetries of the Lagrangian. That is what is postulated by the Higgs mechanism [4, 5, 6], where the existence of a scalar field with non-zero vacuum expectation value reduces the gauge symmetries of the physical vacuum from $\mathrm{SU(3)_C \times SU(2)_L \times U(1)_Y}$ down to $\mathrm{SU(3)_C \times U(1)_{EM}}$, thus leaving the physical vacuum invariant under only the color and electric charges. The $\mathrm{U(1)_{EM}}$ symmetry group requires the existence of a massless gauge boson, the photon ($\gamma$), as the carrier of electromagnetic force. After symmetry breaking the gauge bosons mix to form weak and electromagnetic fields:

$$W_\mu^\pm = \frac{1}{\sqrt{2}} \left( W_\mu^1 \mp W_\mu^2 \right), \tag{1.4}$$

$$Z_\mu = \cos\theta_W W_\mu^3 - \sin\theta_W B_\mu, \tag{1.5}$$

$$A_\mu = \sin\theta_W W_\mu^3 + \cos\theta_W B_\mu \tag{1.6}$$

where $\theta_W$ is the weak mixing angle defined as $\theta_W = \tan^{-1} g^{'}/g$, where $g$ and $g^{'}$ are the coupling constants of $\mathrm{SU(2)_L}$ and $\mathrm{U(1)_Y}$, respectively; $A_\mu$ is the massless electromagnetic photon field ($\gamma$); and $W_\mu^\pm$ and $Z_\mu$ are the charged and neutral weak fields. The mechanism requires the introduction of a complex scalar Higgs doublet. The potential introduced by this field breaks part of the electroweak gauge symmetry, after which only one neutral Higgs scalar $H$ remains. As a result, the $W^\pm$ and $Z$ acquire masses and the photon remains massless.

## 1.2 Open questions and physics beyond the SM

At the current stage all the parameters of the SM have been experimentally measured, the last being the Higgs mass, and the self-consistency of the theory has been tested with electroweak fits [7]. Thus far, the SM proves to be self-consistent and exhibits good agreement between predicted and measured observables. More precise measurements and theoretical calculations are needed in order to reveal the weak points of the SM and thus find indirect hints of new physics. Despite its consistency, the SM remains incomplete as it cannot answer some fundamental questions. I list a few of them below:

- *the hierarchy problem* — the gravitational interaction becomes strong only at the Planck scale, $10^{19}$ GeV, which is much above the electroweak scale of $\sim 100$ GeV. In the SM the Higgs boson mass depends on quantum corrections on the order of the Planck scale, unless there exists some cancellation mechanism, such as supersymmetry [8], extra dimensions [9, 10], or fine-tuning;

- *the grand unification of interactions* — at energies of $\sim 10^{16}$ GeV the coupling constants of the SM gauge symmetries become approximately equal, which suggests there may exist a single gauge symmetry (typically SO(10)) with just one coupling constant [11, 12];

- *the dark matter* — it is not known how to incorporate the observed dark matter into the theory (should it consists of particles) [13];
- *the neutrino masses* — the nature of the neutrino mixing and masses is yet to be determined as well as whether they follow Dirac or Majorana statistics [14];
- *the number of fermion generations* — it is unknown why there are three generations of fermions [15];
- *the matter-antimatter asymmetry* — the observable imbalance between the matter and antimatter in the observable universe hasn't yet been fully explained [16];
- *the vacuum energy* — the SM vacuum energy density is many orders of magnitude higher when compared to astrophysical measurements of the cosmological constant [17, 18];

Moreover, the SM involves 19 parameters, whose values are experimentally determined, but not derived from first principles. To overcome some of the above difficulties many theories beyond the SM have been proposed, such as Supersymmetry (SUSY), Grand Unified Theories (GUT), extra dimensions and others. To date none of them has been experimentally confirmed, nonetheless the searches continue. In the next section an alternative extension of the SM known as Hidden Valleys is introduced.

## 1.3 Hidden Valleys and Long-Lived particles

In many theories like string theory, supersymmetry, grand unification theories etc. one encounters large symmetry groups, which imply the existence of new particles. In these theories the SM symmetry group $\mathrm{SU(3)_C \times SU(2)_L \times U(1)_Y}$ that we observe at the electroweak scale is only a part of a bigger picture. The new interactions between both ordinary and new matter will arise from the larger symmetry groups, and the new states are usually assumed to have masses around the Grand Unification or the Planck scales. However, it is not unreasonable to assume that some of the new particles are lighter, much closer to

the electroweak scale, but there is some barrier that has thus far prevented us from finding them. A new sector of relatively light particles not accessible because of some high energy barrier is called a Hidden Valley [19, 20]. Although, the relevant mass scale of the Hidden Valley is not well specified, it is interesting to study scenarios that may produce visible signals within the reach of the LHC. A good analogy from the SM are the neutrinos, which are somewhat hidden by only interacting via the massive $W$ and $Z$ bosons. There is no reason why the new particles cannot be hidden also.

In Hidden Valley models, the SM gauge group $G_{SM}$ is extended by a symmetry group of the hidden sector $G_v$. All SM particles carry no charges in $G_v$, while all the new particles ($v$-particles) in the hidden sector are charged in $G_v$ and neutral in $G_{SM}$. Higher dimension operators (induced perhaps by a Higgs particle, a $Z^{'}$ or a lightest supersymmetric particle) allow interaction between SM fields and the $v$-particles. One typically assumes that the $G_v$ is a confining, non-abelian group with the $v$-confinement scale $\Lambda_v$, resembling the SM color group, therefore $v$-particles assemble themselves into $G_v$-neutral $v$-hadrons. The $v$-particles may then decay, again via higher dimension operators, to gauge invariant combinations of SM particles. The interactions between the SM and Hidden Valley sector are schematically presented in Fig. 1.2.

There is not a clear minimal representative for Hidden Valley models, but many phenomena are common for a typical $v$-sector. Some examples are listed [21, 22, 23]:

- $v$-hadron production multiplicites at the LHC may be large, especially if $\Lambda_v \ll 1\,\text{TeV}$;
- some $v$-hadrons may be stable, providing dark matter candidates and missing energy signals, while others decay to neutral combinations of SM particles;
- decay lifetimes can vary over many orders of magnitude, some of the $v$-particles may produce displaced vertices;
- some $v$-hadrons decay preferentially to heavy flavor, while others decay more democratically to $f\bar{f}$ states ($f$ is any SM fermion), or $f\bar{f}$ plus another $v$-hadron or other final states.

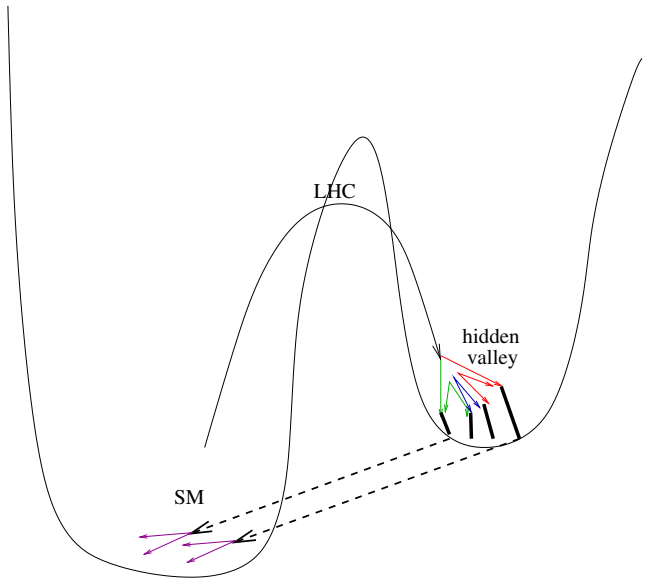


Figure 1.2: Schematic view of production and decay of v-hadrons. If with the energies available at the LHC we may penetrate the barrier and produce v-hadrons, some of them may decay back to SM particles.

If the $v$-particles can be produced at the LHC, they can be detected via missing energy searches, lepton resonance searches, or displaced vertex searches. In this dissertation, I focus on a particular signature where a long-lived $v$-particle decays to quark-antiquark pairs ($q\overline{q}$) at a displaced vertex, while we study all SM quark flavors except the top flavor. Due to the color confinement phenomenon, quarks will hadronize into jets, therefore we will use the term *quark* and *jet* as equivalent from the detection perspective, while a *quark-antiquark pair* will also be called a *dijet*. The analysis presented in the next chapters is potentially sensitive to any heavy particle that decays into a pair of jets at a displaced vertex. However, we study the search sensitivity and optimise the selection using a specific Hidden Valley model as our benchmark. In this model a long-lived, spinless, neutral exotic particle $\mathrm{X}^0$ decays to $q\overline{q}$, the $\mathrm{X}^0$ is pair-produced in the decay of a non-SM Higgs boson, i.e. $\mathrm{H}^0 \to 2\mathrm{X}^0$ , $\mathrm{X}^0 \to q\overline{q}$ [21], and the non-SM Higgs boson is produced through gluon-gluon fusion.

Several other models of new physics predict the existence of massive, long-lived particles, which could manifest themselves through non-prompt decays to dijets. Such scenarios arise, for example, in various supersymmetric (SUSY) scenarios such as "split SUSY" [24] or SUSY

with very weak R-parity violation [25], or Z′ models that contain long-lived neutrinos [26]. The outstanding feature, common in the above models, is the existence of a massive long-lived particle that decays to *at least* two quark jets. The search is therefore designed to look for pairs of hadronic jets that emerge from a common displaced vertex, thus allowing for multiple interpretations.

## 1.4 Previous and present searches

The CDF and D0 collaborations at the Tevatron have performed searches for metastable particles decaying to $b$-quarks [27, 28]. These searches are sensitive to a smaller kinematic phase space region than CMS and explore lower masses of the exotic particles. The ATLAS collaboration at the LHC has performed searches that are sensitive to decay lengths of 1–20 m by exploiting the ATLAS muon spectrometer [29], whilst the search presented here is sensitive to decay lengths typically below 1 m. The ATLAS search required the long-lived particles to be pair-produced, while our search is also sensitive to single or associated production. A previous search by the CMS collaboration for long-lived particles in a similar phase-space region utilized leptonic decay channels [30].

The search presented here has been published as a CMS Physics Analysis Summary [31]. Its journal publication is under way.

# Chapter 2

# The Experiment

## 2.1 The Large Hadron Collider

The Large Hadron Collider (LHC) [32, 33] is a colliding-beam accelerator of circulating beams of protons or lead ions. It sits beneath the French-Swiss border outside of Geneva, in the 27-km-circumference tunnel that was originally used for the Large Electron-Positron collider (LEP). The LHC consists of two beam pipes which house counter-circulating beams.

The protons that collide in the LHC are ionized hydrogen atoms that are bunched in groups of approximately $1.5 \times 10^{11}$ protons. To achieve their final energy of 4 TeV per proton, the proton bunches undergo a series of acceleration steps before being injected into the main LHC ring, as ilustrated in Fig. 2.1.

First, the protons are accelerated in the linear accelerator (LINAC) and injected into the Booster where they reach a kinetic energy of 1.4 GeV. The protons are then injected in the Proton Synchrotron (PS) where the beams are arranged into bunches with 25 ns or 50 ns spacing, and accelerated to 25 GeV. At the next step, proton bunches are injected into the Super Proton Synchrotron (SPS) where they achieve energies of 450 GeV. Finally, the proton bunches are injected into the LHC. Both LHC beams are fed from the SPS through a series of injections until a desired number of bunches is reached in both LHC rings. Then, with accelerating radio-frequency cavities the beams are brought to the desired operating

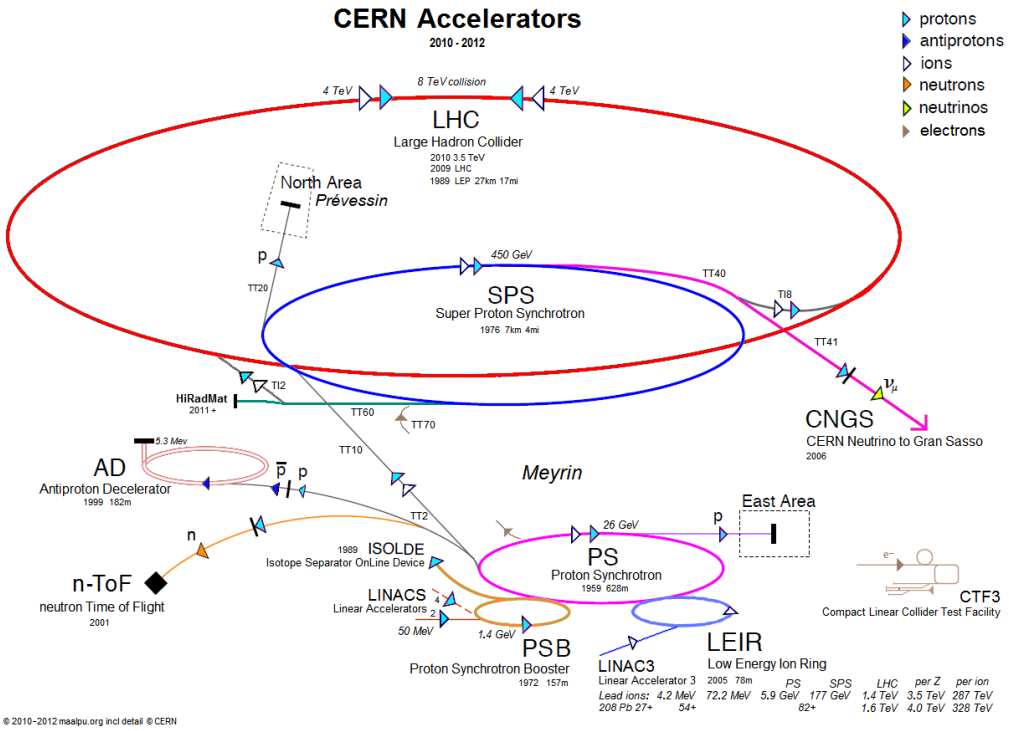


Figure 2.1: A schematic diagram of the LHC accelerator complex.

energies. The center of mass collision energy for which the LHC was designed, namely 14 TeV, is planned to be achieved in 2015. In 2012 the LHC operated at a reduced energy of 4 TeV per proton, for a total center of mass energy of $\sqrt{s} = 8$ TeV.

The beams are steered through the LHC using a series of 1232 superconducting dipole magnets with magnetic fields of up to 5.5 T for beam energy of 4 TeV. In order to provide superconductivity the dipoles are kept at 1.9 K using superfluid helium. In addition to the dipoles, there are 400 quadrupole magnets used for focusing the beams.

The LHC beams are crossed in four sections around the ring to enable collisions of the beams. Each interaction point houses a large detector, two general purpose ones ATLAS and CMS, and two specialized detectors ALICE and LHCb. The ALICE and LHCb experiments took advantage of already available caverns from the LEP experiments, while ATLAS and CMS, located at opposite sides of the LHC ring, as illustrated in Fig. 2.2, are located in caverns built specifically for them.

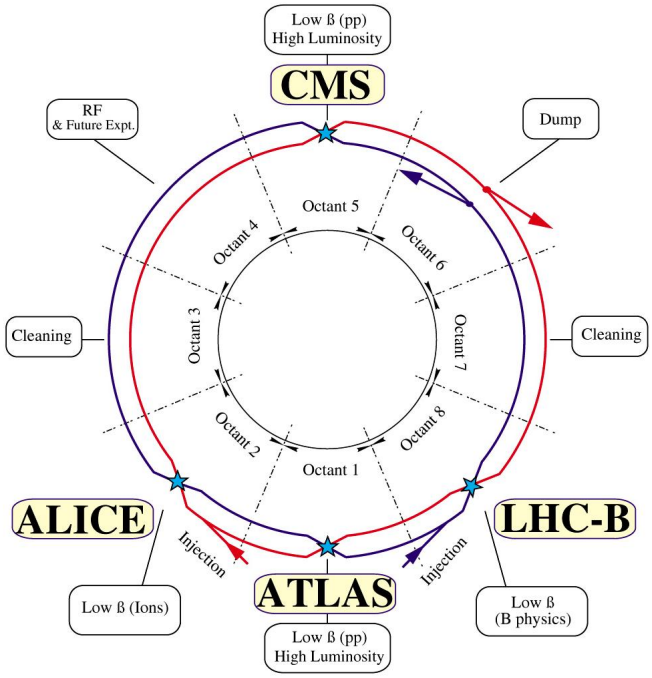


Figure 2.2: The layout of the LHC interaction points.

The instantaneous luminosity of the machine, i.e. the rate of scattering events produced divided by the cross section of the process, is given by [34]:

$$\mathcal{L} = \frac{f n_b N_p^2}{A_{\text{eff}}} \tag{2.1}$$

where $f$ is the orbit frequency ($\sim$11 kHz), $n_b$ is the number of colliding bunch pairs, $N_p$ is the number of protons per bunch, and $A_{\text{eff}}$ is the effective area by which the bunches overlap, transverse to the beam directions.

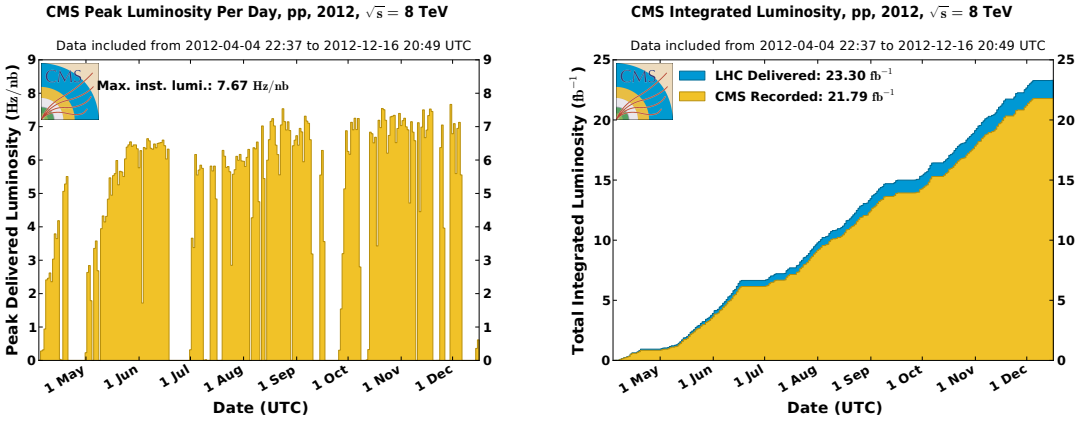


Figure 2.3: The daily peak instantaneous luminosity (left) and the integrated luminosity (right) delivered to the CMS experiment during the 2012 8 TeV proton-proton run.

The peak instantaneous luminosity per bunch during the 2012 LHC run reaches 7 Hz/$\mu$b, Fig. 2.3. Assuming a hard scattering cross section of $\sim$ 70 mb, there are $\sim$30 simultaneous interactions (collisions) for each crossing of the proton bunches. Among multiple proton-proton ($pp$) interactions there is typically only one interaction that has interesting physical properties, while others are minimum bias collisions. We refer to those additional minimum bias collisions as the pileup. The presence of multiple pileup interactions per event poses a significant challenge in the form of difficult event reconstruction and analysis tasks. The total integrated luminosity delivered to the experiments in the 2012 LHC run of 23.3 fb$^{-1}$ is the highest integrated luminosity for a hadron collider to date.

## 2.2 The Compact Muon Solenoid

The Compact Muon Solenoid (CMS) detector is designed to provide efficient identification and measurement of photons, electrons, muons, taus and hadronic showers that emerge from proton-proton collisions. CMS is divided into sub-detector systems, as can be seen in Fig. 2.4. These sub-detectors play complementary roles. The central feature of the CMS apparatus is a superconducting solenoid of 13 m length and 6 m internal diameter. Within the superconducting solenoid volume are a silicon pixel and strip tracker, a lead tungstate crystal electromagnetic calorimeter (ECAL), and a brass/scintillator hadron calorimeter (HCAL). Muons are measured in gas-ionization detectors embedded in the iron return yoke outside the solenoid. Extensive forward calorimetry complements the coverage provided by the barrel and endcap detectors.

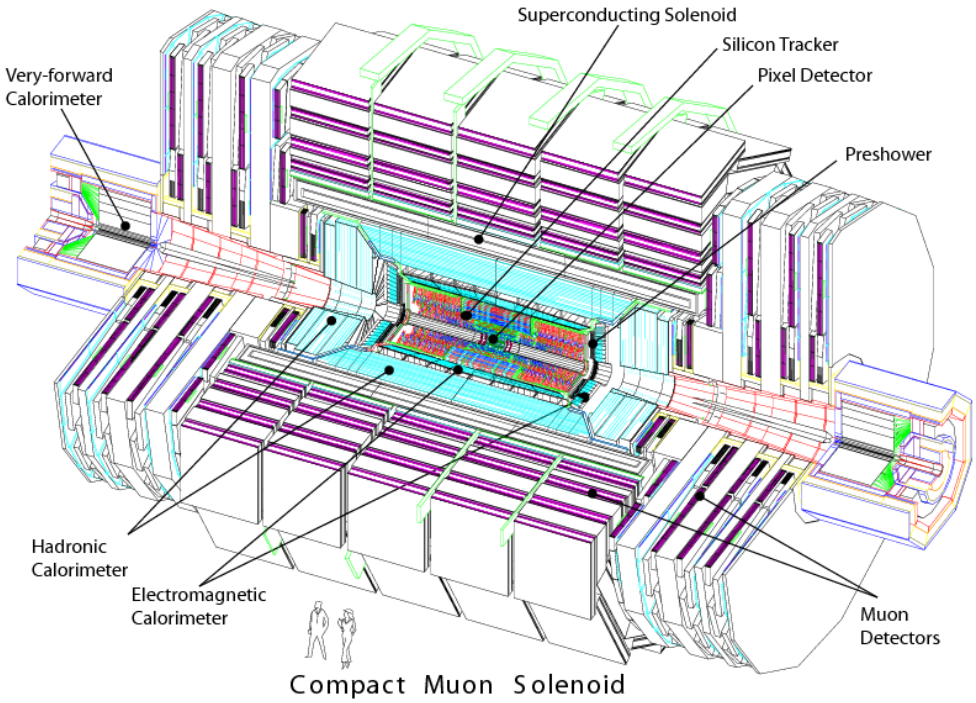


Figure 2.4: The Compact Muon Solenoid detector.

The geometry of the CMS detector is defined such that the $\hat{x}$–axis points toward the center of the ring, and the $\hat{y}$–axis points upward. The $\hat{z}$–axis, then, points in the direction

of the proton beam circulating counterclockwise around the ring (when viewed from above). The angle $\phi$ is measured up from the $\hat{x}$–axis in the $x$-$y$ plane, while the polar angle $\theta$ is measured with respect to the $\hat{z}$–axis. The polar angle is often used to describe the particle's *pseudo-rapidity*, $\eta$, defined as:

$$\eta = -\ln\left(\tan\left(\frac{\theta}{2}\right)\right) \tag{2.2}$$

A more detailed description of the CMS detector can be found in Ref. [35]. The following sections describe the specific features of the CMS detector that are crucial in the search for long-lived neutral particles decaying to jets, namely: the tracking system, the particle-flow reconstruction and the jet reconstruction algorithm.

### 2.2.1 Tracking system

The tracker, which is the innermost detector system of the CMS detector, has a length of 5.8 m and a diameter of 2.5 m. It is immersed in a coaxial magnetic field of 3.8 T provided by the CMS solenoid. A schematic drawing of the CMS tracker is shown in Fig. 2.5. It comprises a silicon pixel detector with three barrel layers at radii between 4.4 cm and 10.2 cm and a silicon strip tracker with ten barrel detection layers extending outwards to a radius of 1.1 m. Each system is completed by endcaps, which consist of two disks in the pixel detector and three plus nine disks in the strip tracker on each side of the barrel, extending the acceptance of the tracker up to a pseudorapidity of $|\eta| < 2.5$.

The track reconstruction sequence is divided into five parts:

- **Local reconstruction** consists of clustering into *hits* the strip and pixel signals produced by charged particles on the silicon detectors of the tracking system. The positions of the hits are estimated along with the corresponding uncertainties;
- **Seed generation** provides initial track candidates for the full track reconstruction. A seed defines the initial trajectory parameters and errors;
- **Pattern recognition** is based on a global Kalman filter [36] and is responsible for finding the track candidates that correspond to charged particles of interest. The tra-

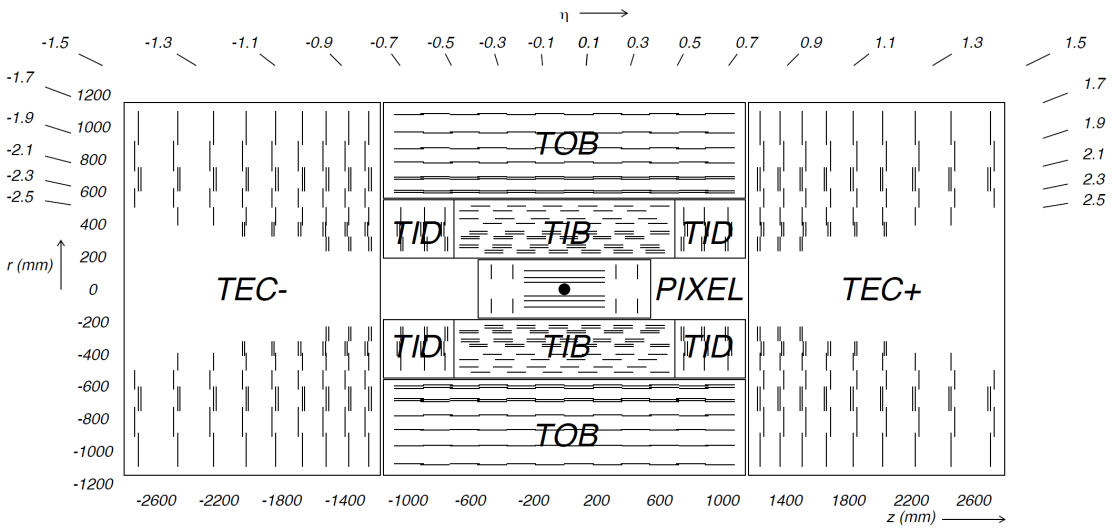


Figure 2.5: Schematic cross section through the CMS tracker. Each line represents a detector module. Double lines indicate back-to-back modules which deliver stereo hits.

jectory parameters are updated whenever a *hit* is found along the trajectory. Because the trajectories are built in parallel and allowed to share position measurements, this step is also responsible for removing duplicates (hits assigned to more than one track);

- **Final track fitting** module estimates the final parameters of the trajectories with ultimate precision;

- **Track selection** rejects fake tracks by requiring that all tracks satisfy a minimal set of quality criteria.

To improve the track finding efficiency, the above reconstruction procedure is performed in six iterations. After each iteration, the hits used for the best quality tracks (high purity tracks) are locked and removed from the pool of hits available for the next iterations. The iterations differ from each other mainly in how they seed the tracks. The $0^{\text{th}}$ iteration uses pixel-triplet seeds (formed from hits in 3 pixel layers), while the $1^{\text{st}}$ iteration uses pixel-pair seeding (formed from hits in any 2 pixel layers), allowing it to recover tracks with missing pixel hits due to inefficiency or acceptance. These two iterations suffice to reconstruct the vast majority of moderately high $p_T$ tracks (>1 GeV) originating from the production

vertex. The 2nd and 3rd iterations also use pixel seeding, but since many of the tracker hits have already been locked by the time they run, they can use a very low $p_T$ cut or a rather loose primary vertex constraint. Finally, the $4^{th}$ and $5^{th}$ iterations seed the tracks in the strip tracker double-layers, which provide 3D hits by combining information from mono and stereo hits. This allows them to find particles produced outside the volume of the pixel tracker. The procedure has been optimized for using as many tracker hits as possible while keeping the rate of fake tracks negligible.

The CMS tracker provides an impact parameter resolution of $\sim$15 $\mu$m and a transverse momentum ($p_{\mathrm{T}}$) resolution of about 1.5% for 100 GeV particles. The track reconstruction algorithms are able to reconstruct displaced tracks with transverse impact parameters up to $\approx$30 cm from particles decaying up to $\approx$60 cm from the beam line. The performance of the track reconstruction algorithms has been studied with data [37]. The silicon tracker is also used to reconstruct the positions of primary vertices with a precision of $\sim$20 $\mu$m in each dimension.

### 2.2.2 Particle-Flow (PF) reconstruction

The global event reconstruction (also called particle-flow event reconstruction [38, 39]) is designed to reconstruct and identify each particle in the event using an optimized combination of all subdetector information. Fig. 2.6 presents schematically how various types of particles are reconstructed with the CMS detector.

In this process, the identification of the particle type (photon, electron, muon, charged hadron, neutral hadron) plays an important role in the determination of the particle direction and energy. Photons are identified as ECAL energy clusters not linked to the extrapolation of any charged particle trajectory to the ECAL. Electrons are identified as primary charged particle tracks that point to ECAL energy clutsers. The particle-flow algorithm takes into account the energies of the nearby clusters consistent with the bremsstrahlung photons. Muons are identified as tracks in the central tracker matched to either a track or several hits in the muon system, associated with an energy deficit in the calorimeters.

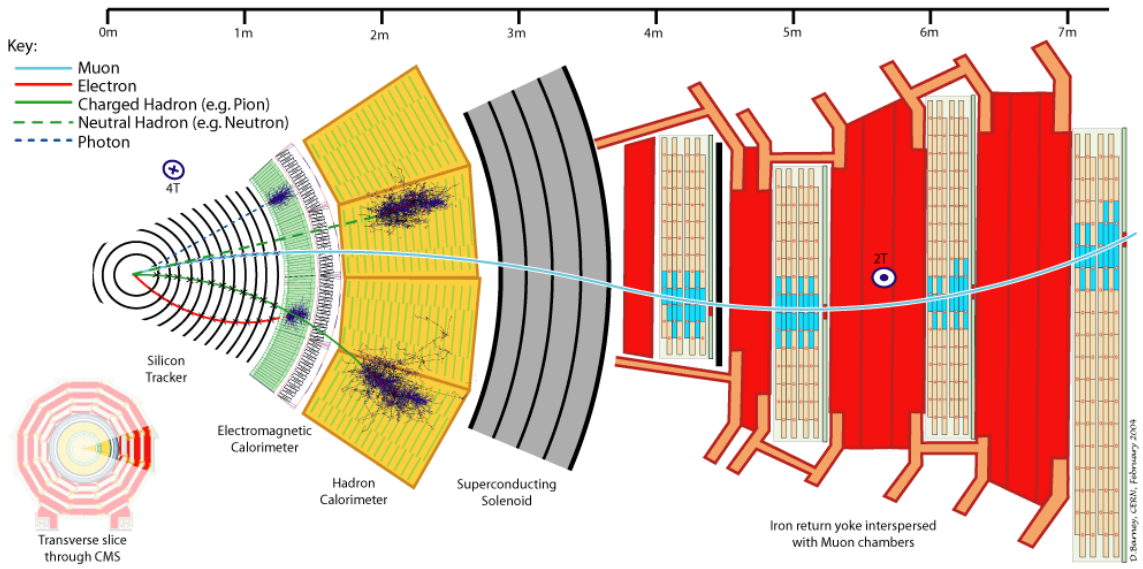


Figure 2.6: Transverse slice of the CMS detector. For each type of particle, namely muon, electron, photon and the neutral or charged hadron, the characteristic signatures left in the relevant subdetectors are shown.

Charged hadrons are identified as charged particle tracks identified as neither electrons nor muons. Finally, neutral hadrons are identified as HCAL energy clusters not linked to any charged hadron trajectory, or as ECAL and HCAL energy excesses with respect to the expected charged hadron energy deposit.

The energy of photons is directly obtained from the ECAL measurement, corrected for zero-suppression effects. The energy of electrons is determined from a combination of the track momentum at the main interaction vertex, the corresponding ECAL cluster energy, and the energy sum of all bremsstrahlung photons attached to the track. The energy of muons is obtained from the corresponding track momentum. The energy of charged hadrons is determined from a combination of the track momentum and the corresponding ECAL and HCAL energy, corrected for zero-suppression effects, and calibrated for the nonlinear response of the calorimeters. Finally, the energy of neutral hadrons is obtained from the corresponding calibrated ECAL and HCAL energy.

### 2.2.3 Jet reconstruction

For each event, hadronic jets are clustered from the particles reconstructed with the PF algorithm with the infrared and collinear safe anti-$k_{\mathrm{t}}$ algorithm operated with a size parameter $R$ of 0.5 [40]. The size parameter requires that all the jet particles have $\Delta R \leq 0.5$ relative to the jet momentum vector, where $\Delta R = \sqrt{(\Delta\phi)^2 + (\Delta\eta)^2}$. The jet momentum is determined as a vectorial sum of all particle momenta in this jet. MC simulation studies indicate that for jets originating at the event primary vertex the jet momentum is within 5% to 10% of the true momentum over the whole $p_{\mathrm{T}}$ spectrum and detector acceptance. When the jet origin is significantly displaced from the event primary vertex, the reduced charged particle efficiency results in additional underestimation of the jet momentum. For displaced jets originating within the volume of the CMS tracker the jet momentum is underestimated in the simulation by up to 10% (the effect is explained in more detail in Section 5.8).

## 2.3 Trigger

The high instantaneous luminosity at the LHC together with limitations on the storage space available for CMS data necessitate the existence of a trigger. The aim of the trigger is to reduce the rate of collision events from $\sim$ 15 MHz, delivered by the LHC, to $\sim$ 500 Hz that will be stored for further analysis, while keeping the events of potential physics interest. The details of the CMS trigger design and implementation are described in [41], only the basic concepts are explained here.

The CMS trigger system consists of two parts: "the Level One" (L1) and "the High Level Trigger" (HLT). The L1 is a set of electronics operating at 40 MHz and has a latency of 3 $\mu s$. During this time only simplified objects are reconstructed from the detector readouts using fast electronics. They include L1 muon, photon, electron, and jet candidates, as well as an energy sum of all jets in the event and the missing transverse energy. Only the objects above, or combinations of them, are used to make acceptance decisions. The maximum allowed output rate of the L1 trigger part is 100 kHz. Events passing the L1

requirements are processed by the HLT with software reconstruction sequences that closely approximate the offline reconstruction. The mean processing time per event is 50 ms. There are about 500 various HLT trigger paths, each of which can make an acceptance decision based on the reconstructed objects (jets, leptons, missing energy). The number of trigger paths approximately corresponds to the number of searches and measurements pursued by the CMS collaboration. Frequently the physics objects upon which the decisions are made overlap between the triggers, in which case the reconstruction is performed only once.

### 2.3.1 Trigger for long-lived particles decaying to dijets

A dedicated trigger has been designed to accept events that contain long-lived particles decaying to dijets. The underlying idea behind such a trigger is not to reconstruct dijets associated with a displaced vertex, because such a procedure is too complicated to be executed at the HLT stage, but rather to simply reject events where all the jets are produced promptly at the collision point. The rate limitations (up to 1 Hz imposed by the CMS collaboration) together with the limited execution time (up to 5 ms on average for a single trigger path) resulted in a trigger that consists of the following filters:

1. Scalar transverse energy sum of all the L1 jets in the event, $H_T$, above 150 GeV, which is the lowest threshold allowed by L1 rate limitations;

2. Scalar transverse energy sum of all the HLT jets in the event, $H_T$, above 300 GeV. The jets at L1 are determined with large uncertainties. Imposing a requirement twice as large at the HLT guarantees very high L1 efficiency and therefore reduces the dependence of the further analysis on the L1 trigger performance;

3. At least two jets that have transverse momenta, $p_T > 60$ GeV and pseudorapidity $|\eta| < 2$. This requirement selects jets that are central and well within the acceptance of the CMS tracker;

4. At least two of the jets selected in step 3 are required to have not more than two tracks that have impact parameters smaller than 300 $\mu$m. This requirement rejects

many promptly produced jets, which typically have many tracks with small impact parameters;

5. For at least two of the jets selected in step 4 the jet energy fraction carried by the tracks that have transverse impact parameters smaller than 500 $\mu$m is required to be smaller than 15%. This requirement also suppresses promptly produced jets.

In addition to the trigger just described, a control trigger has been designed, which consists of the same steps, but is modified such that the steps 3 through 5 require that only one jet fulfills the corresponding requirement. The two triggers are then called *double displaced jet* and *single displaced jet* triggers. Due to HLT rate limitations the *single* trigger was prescaled. Both triggers were active during the entire 2012 LHC run and the number of events collected by CMS together with the integrated luminosity is summarized in Table 2.1. Data collected by the double displaced jet trigger, where the presence of two triggering

Table 2.1: Displaced jet triggers active in 2012 LHC run.

| trigger name | prescale factor | $\mathcal{L}$ [fb$^{-1}$ ] | N events [1e6] |
|---|---|---|---|
| single displaced jet | 100-120 | 0.18 | 0.5 |
| double displaced jet | 1 | 18.5 | 1.9 |

jets is required, is used to search for our signal, while data collected by the single jet trigger is used as a prescaled control sample.

## 2.4 Event simulation

Simulated events, also known as Monte Carlo (MC) events, are crucial when designing and conducting a search. Prior to the analysis of the LHC data both simulated signal and SM background events are typically used to design the event reconstruction, determine the optimal event selection, estimate the signal efficiency and the background rate.

When generating the simulated events, partons from distribution functions (CTEQ [42]) undergo hard scattering in PYTHIA [43]. The parton showers are then hadronized again with

PYTHIA and the unstable particles are left to decay. The particles outgoing from the collision point are then propagated through the CMS detector using GEANT4 [44], which provides a full description of the detector geometry and simulates the interactions of particles with the detector material. The energy deposits are digitized to emulate the response of the detector electronics followed by event reconstruction, as for data. Additionally, in order to reproduce the condition of multiple simultaneous interactions occurring in the same crossing of the bunches, a number of simulated hard-scattering events are overlaid on top of the primary simulated event. The distribution of the number of simultaneous interactions overlaid in the MC data samples is chosen such that it approximates the LHC running conditions.

For the purpose of this search, signal MC simulation samples are generated to simulate non-SM Higgs ($H^0$) production through gluon fusion ($gg \to H^0$). Subsequently the $H^0$ is forced to decay to two long-lived, spin 0, exotic particles ($H^0 \to 2X^0$), each of which then decays to quark-antiquark pairs ($X^0 \to q\bar{q}$). The long-lived exotic $X^0$ decays to any flavor $q\bar{q}$ pair, excluding $t\bar{t}$, with equal probability. Samples with different combinations of $H^0$ masses ($M_{H^0} = 120, 200, 400, 1000$ GeV) and $X^0$ boson masses ($M_{X^0} = 20, 50, 150, 350$ GeV) are generated. These are listed in Table 2.2.

Table 2.2: Simulated signal samples used in the analysis. The masses of the $H^0$ and $X^0$ bosons are given, as is the mean proper decay length of the $X^0$ boson.

| $M_{H^0}$ (GeV) | $M_{X^0}$ (GeV) | $c\tau$ (cm) |
|---|---|---|
| 1000 | 350 | 3.5, 35, 350 |
| 1000 | 150 | 1, 10, 100 |
| 1000 | 50 | 0.4, 4, 40 |
| 1000 | 20 | 0.15, 1.5, 15 |
| 400 | 150 | 4, 40, 400 |
| 400 | 50 | 0.8, 8, 80 |
| 400 | 20 | 0.4, 4, 40 |
| 200 | 50 | 2, 20, 200 |
| 200 | 20 | 0.7, 7, 70 |
| 120 | 50 | 5, 50, 500 |
| 120 | 20 | 1.3, 13, 130 |

The $X^0$ boson lifetimes used in these samples are chosen to give mean transverse decay

lengths of approximately 3 cm, 30 cm and 300 cm in the laboratory frame. Such a selection of laboratory frame lifetimes is chosen in order to fully explore the capabilities of the CMS detector for reconstructing long-lived particles. The spectra of the simulated $H^0$ and $X^0$ transverse momenta, $p_T$, and the $X^0$ pseudorapidity, $\eta$, are presented in Fig. 2.7 for selected signal models. An example of a fully reconstructed simulated signal event is presented in

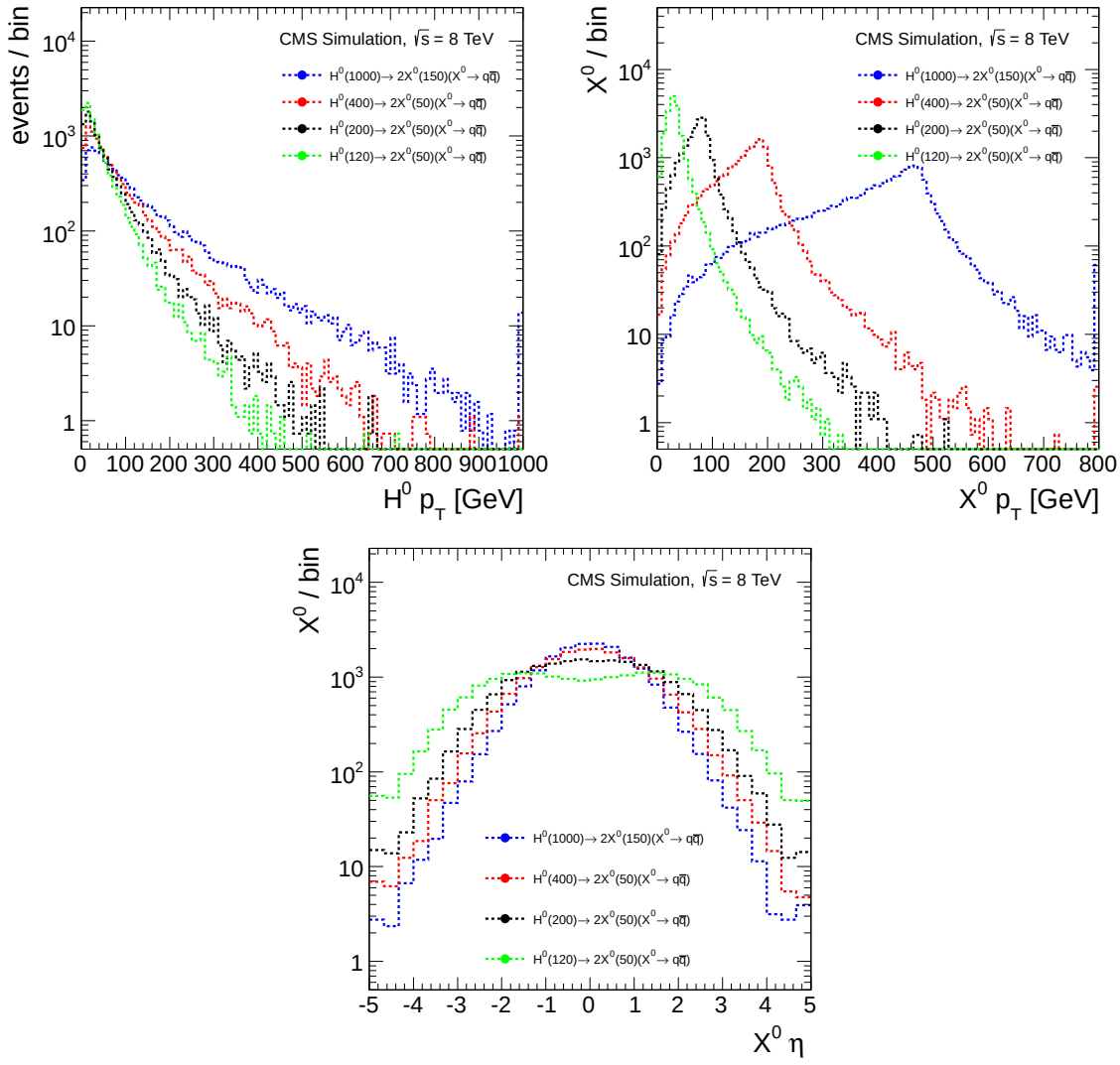


Figure 2.7: Generated $H^0$ $p_T$ and $X^0$ $p_T$ and $\eta$ distributions for selected signal models.

Fig. 2.8.

The main background to this search consists of events containing hadronic jets. Many

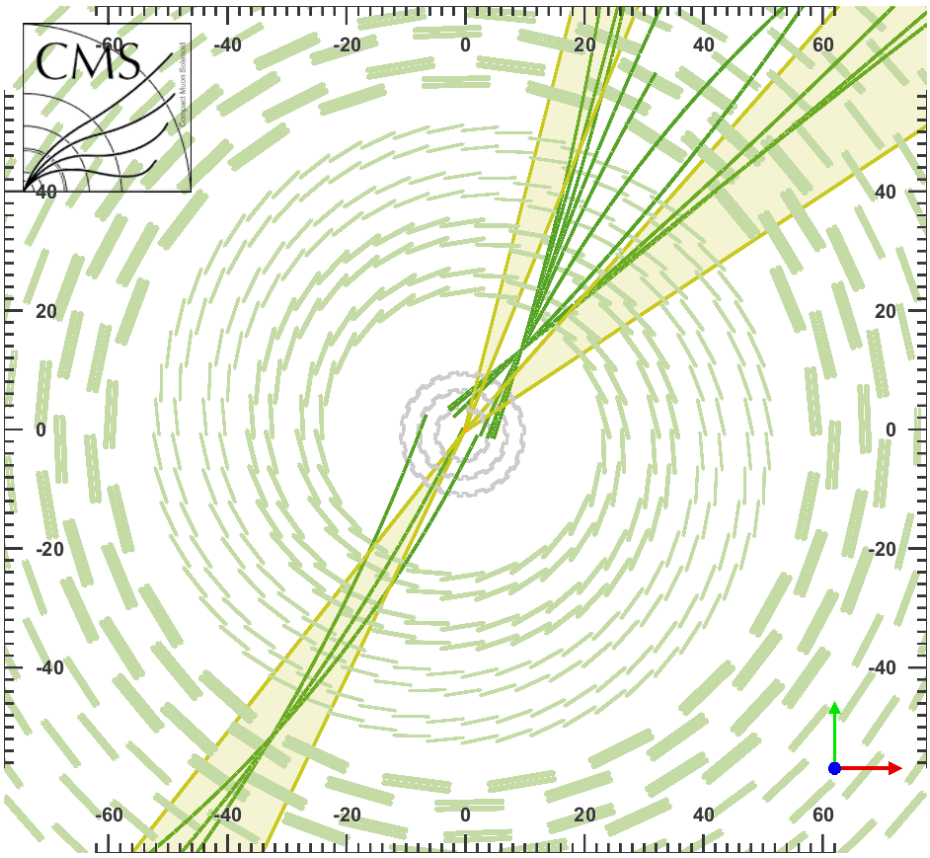


Figure 2.8: CMS event display of an example simulated signal event with a dijet pair originating from a transversely displaced secondary vertex. The event is presented in the plane transverse to the LHC beam line. The concentric layers of detectors (grey or light green) show the tracker detector modules, the yellow cones correspond to reconstructed jets, while the thick green lines are charged particle trajectories. A displaced secondary vertex is clearly visible with a dijet pair moving towards top-right corner of the picture. The axis labels use cm units.

SM processes produce events with multiple jets. Given the considerable phase space and the large SM production cross sections, the most significant background is expected to arise from QCD events. The corresponding simulated samples are listed in Table 2.3. The samples are binned in terms of the transverse momentum transfer between the colliding partons, $\hat{p_T}$. The resulting transverse sum of the jets, $H_T$, for these events corresponds to approximately twice the value of $\hat{p_T}$. For each simulated background sample, the number of events passing the signal trigger scaled to the total integrated luminosity is shown. The per-event weight factors that need to be applied in order to compare the simulated samples with the data are also given. These arise simply from the cross section of the process, the total integrated luminosity, and the number of events simulated for each dataset. The weight factors for samples with $\hat{p_T}$ below 470 GeV are significantly above unity, therefore the number of simulated events in this region is insufficient to compare with data. Since the background significantly decreases with increased $\hat{p_T}$, we do not consider samples with $\hat{p_T}$ higher than 800 GeV. For QCD events with $\hat{p_T}$ below 80 GeV, the small efficiency for passing the $H_T$ >300 GeV trigger requirement makes the low $\hat{p_T}$ contribution negligible.

Table 2.3: Simulated background samples used in the analysis.

| Dataset name | cross section (pb) | N events passing the trigger / 18.5 fb$^{-1}$ | Per event weight factor |
|---|---|---|---|
| QCD (600< $\hat{p_T}$ <800 GeV) | $2.70 \times 10^1$ | $4.5 \times 10^2$ | 0.1 |
| QCD (470< $\hat{p_T}$ <600 GeV) | $1.14 \times 10^2$ | $1.7 \times 10^3$ | 0.6 |
| QCD (300< $\hat{p_T}$ <470 GeV) | $1.76 \times 10^3$ | $2.6 \times 10^4$ | 5.5 |
| QCD (170< $\hat{p_T}$ <300 GeV) | $3.41 \times 10^4$ | $5.2 \times 10^5$ | $1.1 \times 10^2$ |
| QCD (120< $\hat{p_T}$ <170 GeV) | $1.56 \times 10^5$ | $7.5 \times 10^5$ | $4.8 \times 10^2$ |
| QCD (80< $\hat{p_T}$ <120 GeV) | $1.03 \times 10^6$ | $4.8 \times 10^5$ | $3.2 \times 10^3$ |
| QCD (50< $\hat{p_T}$ <80 GeV) | $8.15 \times 10^6$ | $1.1 \times 10^5$ | $2.5 \times 10^4$ |

# Chapter 3

# Event Selection

This chapter begins by determining the sensitivity of the search strategy as a function of the masses and the lifetimes of the exotic particles. That discussion is followed by a description of the reconstruction of long-lived dijet candidates. The signal and background candidates are examined using simulated samples followed by a correlation study between the discrimination criteria.

## 3.1 Signal model sensitivity

### 3.1.1 $H^0$ mass

The $H^0$ mass range sensitivity is most affected by the $H_T > 300\,\text{GeV}$ requirement imposed by the trigger. In order to minimize the effects of the trigger turn-on curve, we require $H_T > 325\,\text{GeV}$ in the offline reconstruction.

Fig. 3.1 presents the offline reconstructed $H_T$ distributions for selected signal models; all available $H^0$ mass points are shown. The $H_T > 325\,\text{GeV}$ requirement reduces the sensitivity of the search in the low mass region of the exotic $H^0$, therefore we analyze further only those signal models where the mass of the $H^0$ is 200 GeV or higher.

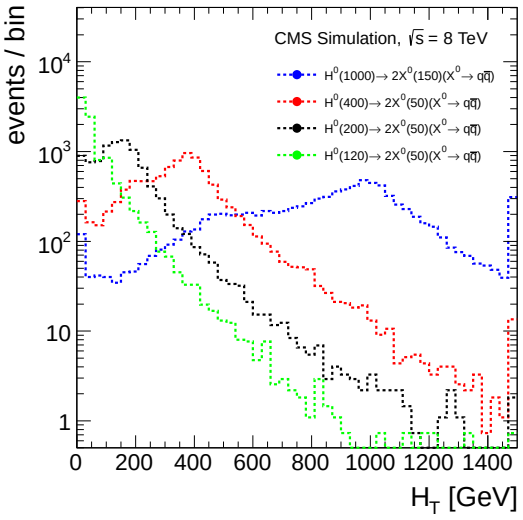


Figure 3.1: $H_T$ distributions for the benchmark signal models.

### 3.1.2 $X^0$ mass given the $H^0$ mass

In this search we aim to reconstruct displaced dijet candidates originating from a common displaced vertex using pairs of jets that need to fall within the tracker acceptance ($|\eta| < 2$). The jets are reconstructed with an anti-k$_T$ algorithm operated with a size parameter $R$ of 0.5 [40], which also determines the minimal angular distance between the jets reconstructed in the event. In order to reconstruct two distinct jets with this algorithm the opening angle between the two quarks needs to be above 0.5 radians. Fig. 3.2 presents the opening angle distributions between the two quarks originating from $X^0 \to q\bar{q}$ decay for signal models with $M_{H^0}$= 200, 400, and 1000 GeV.

The efficiency for reconstructing a pair of jets corresponding to the $X^0 \to q\bar{q}$ decay using the anti-k$_T$ algorithm with a 0.5 radius as a function of the opening angle of the quark pair is shown in Fig. 3.3. Both jets are required to have $p_T > 60$ GeV and $|\eta| < 2$, which causes the efficiency to be reduced for lower $H^0$ masses.

The dijet analysis is therefore sensitive to long-lived $X^0$ particles with masses such that a significant fraction of the candidates have opening angles above 0.5, namely:

- $M_{X^0}$ between 150-350 GeV for $M_{H^0}$=1000 GeV

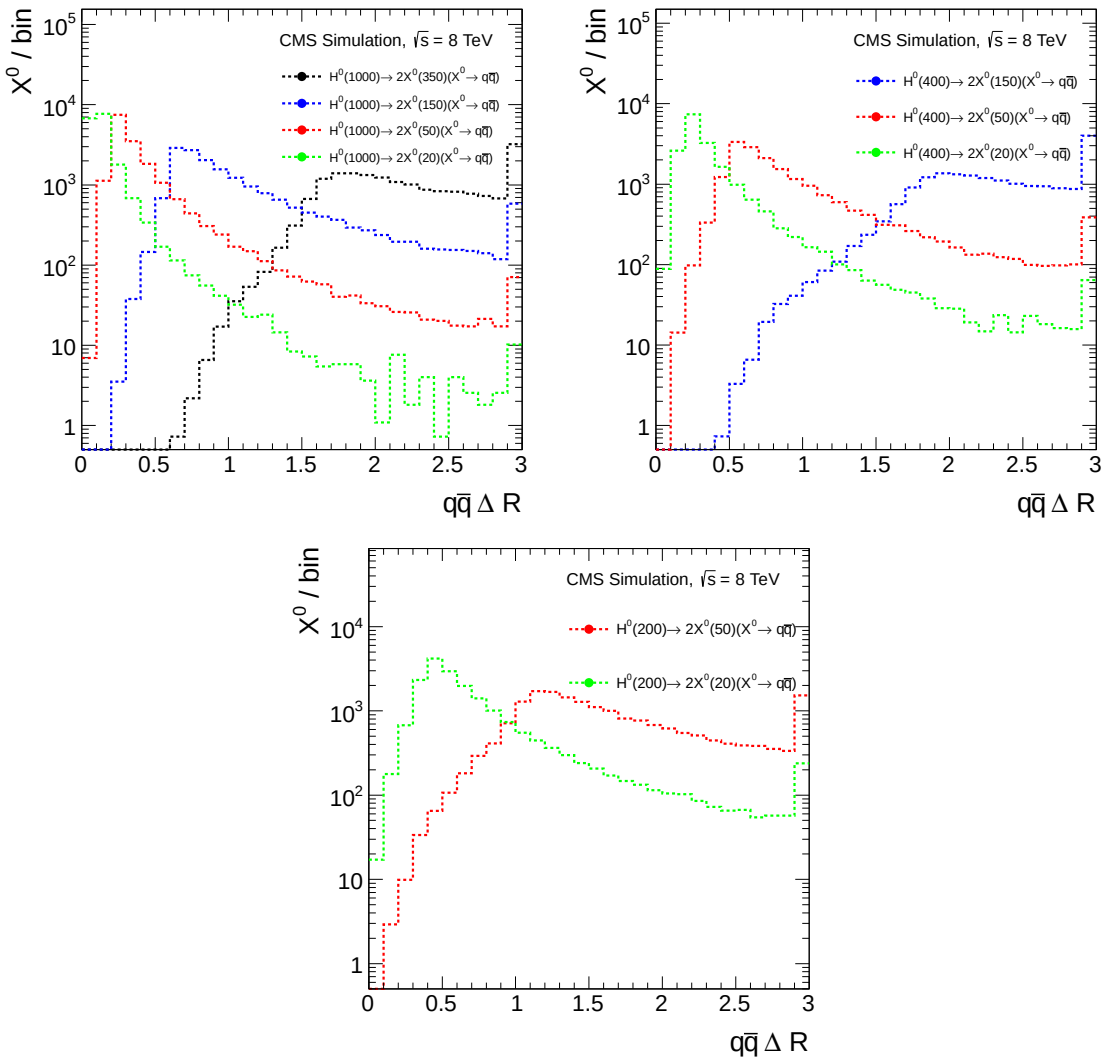


Figure 3.2: Opening angle distributions of the $q\bar{q}$ pair originating from the $X^0 \to q\bar{q}$ decay as a function of $H^0$ and $X^0$ particles masses.

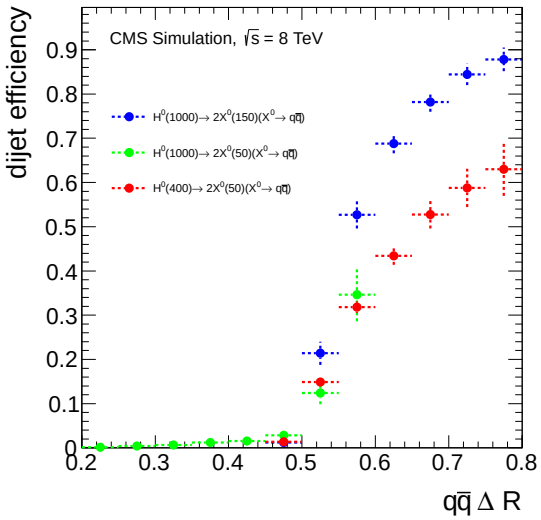


Figure 3.3: Dijet reconstruction efficiency as a function of the quark-pair opening angle for jets reconstructed with an anti-k$_T$ algorithm operated with a cone size of 0.5. Both reconstructed jets are required to have $p_T > 60\,\text{GeV}$ and $|\eta| < 2$.

- $M_{\text{X}^0}$ between 50-150 GeV for $M_{\text{H}^0}$=400 GeV
- $M_{\text{X}^0}$=50 GeV for $M_{\text{H}^0}$=200 GeV

## 3.2 Reconstruction

In the reconstruction process described below, we identify characteristic variables of the long-lived dijet candidates that provide signal-to-background discrimination using simulated MC samples. There is no SM process giving rise to displaced dijet pairs. Jets may, however, contain displaced (high impact parameter) tracks originating from B meson decays, nuclear interactions of charged particles with the tracker material, $\text{K}^0_\text{S}$ and $\Lambda^0$ decays, etc. These tracks, if present for two distinct jets, may then cross at a displaced location and mimic a common dijet vertex.

We apply a trigger that requires $H_T$ >300 GeV, but does not require jets having few low impact parameter tracks. All figures in this section that show signal and background MC distributions are scaled to the total available luminosity of 18.5 fb$^{-1}$. The cross section of the signal process has been set to 10 $\mu$b for purposes of illustration.

LHC collision events usually contain many primary vertices corresponding to multiple proton-proton collisions occurring in the same bunch crossing. Among the set of primary vertices, we select the one whose tracks have the highest squared transverse momentum sum. The primary vertex position is then used as a reference point for computing decay lengths and impact parameters. The impact of a wrong primary vertex assignment on the background yield and the signal reconstruction efficiency is discussed in Section 5.4.

We search for dijet candidates by selecting every pair of jets, where both jets are required to have $p_T > 60\,\text{GeV}$ and $|\eta| < 2$. The signal dijet candidates are limited to those where both reconstructed jets are matched within a cone of $\Delta R = 0.5$ to generator level quarks originating from the $X^0$ boson decay. Applying this requirement does not change the signal reconstruction efficiency once the full selection is applied.

Among the jet constituents charged tracks are associated within $\Delta R = 0.5$ cone to each jet. The track momentum vector used for the association is evaluated at the point of closest approach to the beam line. Only tracks with $p_T > 1\,\text{GeV}$ are considered. Tracks with lower transverse momenta do not reach the calorimeter system due their strong deflection in the CMS magnetic field. Among the tracks we select a set of displaced tracks defined as those with a transverse impact parameter with respect to the primary vertex greater than $500\,\mu\text{m}$, which is large enough to exclude most of the B hadron decay products. The individual impact parameters are signed with the sign of the scalar product between the dijet momentum vector and the impact parameter vector in the transverse plane. For each jet we also repeat the calculation of variables used in the displaced jet trigger using offline reconstruction, namely:

- the number of prompt tracks - for tracks with impact parameter in 3 dimensions smaller than $300\,\mu\text{m}$, Fig. 3.4;
- the jet energy fraction carried by prompt tracks - for tracks with transverse impact parameter smaller than $500\,\mu\text{m}$, Fig. 3.4.

Secondary vertices are sought among the displaced tracks associated with each dijet pair

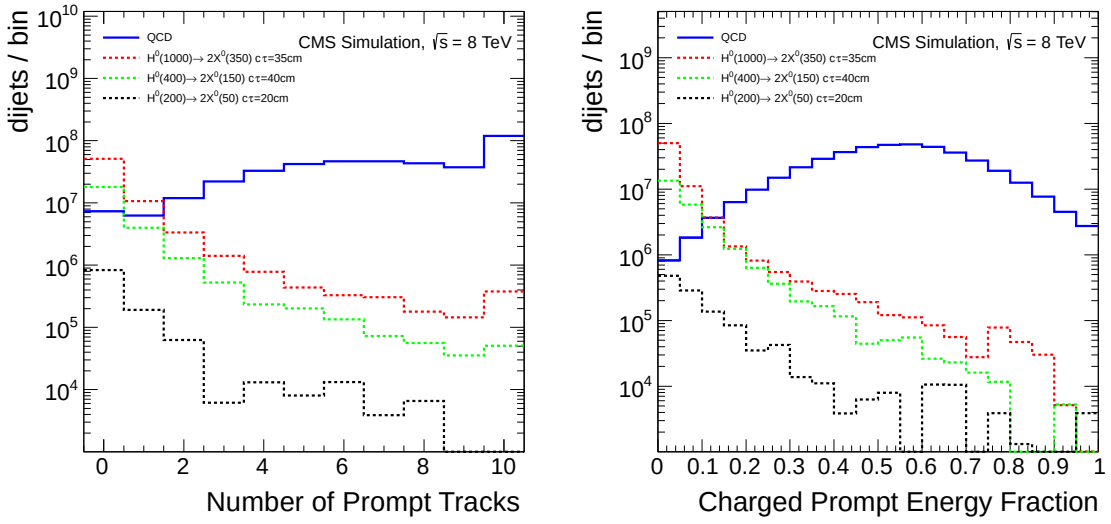


Figure 3.4: Number of prompt tracks associated to the jet and charged prompt jet energy fraction for signal and background MC samples. There are two jets in a dijet pair, however the distributions for both jets are identical. We present the distributions for the lower $p_T$ jet in the dijet pair.

using two different algorithms.

The Vertex Fitter [45] performs an iterative least-squares estimate of the secondary vertex position. The consecutive iterations down-weight tracks that seem inconsistent with the fitted vertex position until an optimum is found. The secondary dijet vertex is required to have a chisquared per degree of freedom $\chi^2/\text{dof} < 5$. Additionally, for compatibility with the displaced dijet hypothesis, we require that at least one track from each jet be included in the secondary vertex. This requirement greatly reduces the background contribution from nuclear interaction vertices. The nuclear interaction vertices are characterized by low invariant mass of the outgoing tracks, making it unlikely that the outgoing tracks are associated with two distinct jets. The following quantities obtained from the vertex fit, with plots presented in Fig. 3.6, provide discrimination between signal and background:

- vertex track multiplicity;
- fraction of tracks assigned to the vertex with a positive value of signed impact parameter;

- invariant mass of the vertex tracks (vertex mass);
- $p_T$ of the vertex tracks (vertex $p_T$);
- $L_{xy}$ significance - where $L_{xy}$ is the distance between secondary and primary vertices in the transverse plane;
- number of missing tracker hits per track after the vertex position - each track in CMS is reconstructed from hits in the silicon tracker using a Kalman Filter algorithm [46]. The algorithm propagates track seeds through the CMS tracker in the direction from the beam line towards the calorimeters. Whenever a hit is found along the trajectory the track parameters are updated, while occasional missing measurements are allowed. For each of the vertex tracks, we compute a number of missing tracker measurements starting from the secondary vertex position until the innermost hit of the track. We then average the missing measurements over the vertex tracks. The fitted vertex position may be significantly closer to the beam line than the track production point, if the track comes from a nuclear interaction or a $V^0$ decay. An example of a fake secondary vertex (SV) that can be rejected by requiring a small number of missing tracker hits after the vertex position is shown in Fig. 3.5.

In the second algorithm we search for clustering of the $L_{xy}$ values from the tracks in the jets. For each of the displaced tracks associated with either jet, a decay point consistent with the displaced dijet hypothesis is determined. As schematically presented in Fig. 3.7 such a point can be obtained as the crossing point of the particle trajectory and a straight line drawn from the primary vertex in the direction of the dijet momentum. Information about the production point for each track is then used to compute an expected path length in the transverse plane, $L_{xy}^{\text{exp}}$. For high momentum tracks the trajectory in the transverse plane is a straight line, therefore the decay point can be determined from the crossing point between two lines, and the expected path length is simply:

$$L_{xy}^{\text{exp}} = \frac{d_{xy}}{\sin(\phi_{\text{track}} - \phi_{\text{dijet}})} \tag{3.1}$$

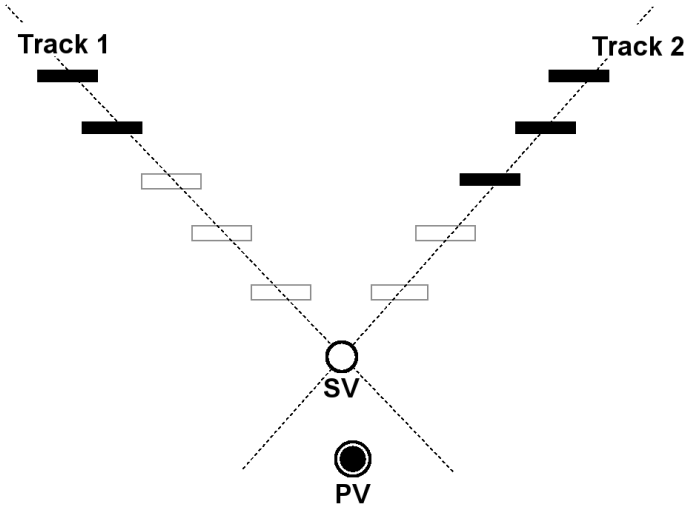


Figure 3.5: An example of a fake secondary vertex with multiple missing hits after the secondary vertex position. The rectangular tracking modules are filled if a hit is found and empty if there is no hit present. The two tracks that form a secondary vertex have three and two missing measurements after the secondary vertex position. Such a secondary vertex may be found e.g. if the two tracks originate from two distinct nuclear interaction vertices; if one track comes from a nuclear interaction vertex while the other comes from a pileup interaction; etc.

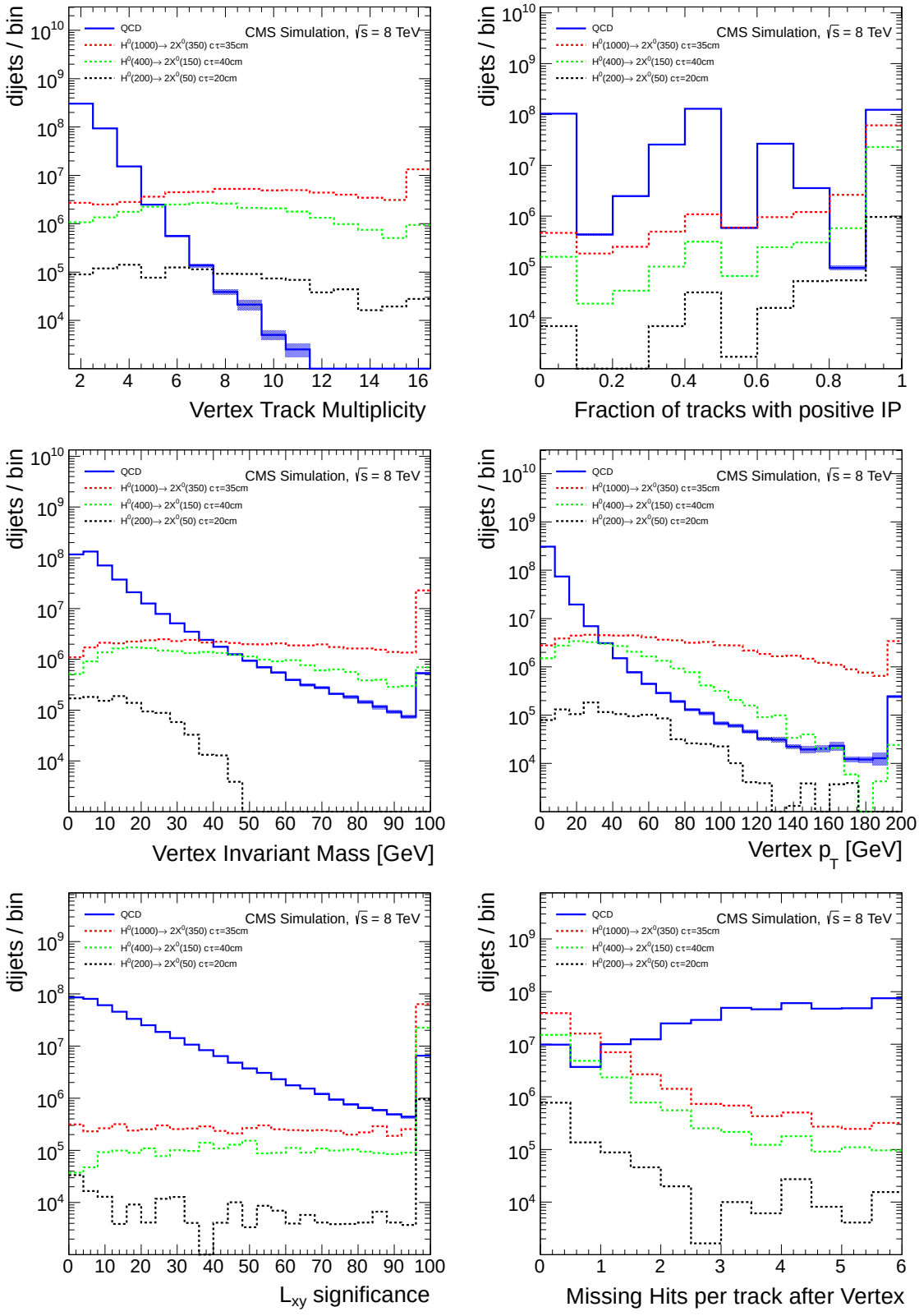


Figure 3.6: Secondary vertex discrimination variables for signal and background MC samples.

where $d_{xy}$ is the transverse impact parameter and $\phi$ is the azimuthal angle. However, in the presence of an axial magnetic field, the formula above is not valid as a result of curvature. In order to find the expected path length in such cases, we find a corresponding crossing point for the track helix with a radius $R$. Since we consider only tracks with $p_T$ >1 GeV, which translates to a helix radius $R > 80\,\text{cm}$, the calculation is limited to first order in $d_{xy}/R$. A line drawn from the primary vertex along the dijet momentum crosses the helix twice, yielding two solutions, although only one of them behaves properly when $R \to \infty$ and reduces to Eq. 3.1. Nevertheless, we consider two separate cases:

- primary vertex lies inside the track helix:

$$L_{xy}^{\text{exp}} = \frac{d_{xy}}{\sin\left(\phi_{\text{track}} - \phi_{\text{dijet}}\right)} \left(1 - \frac{d_{xy}}{R}\right) + o\left(\left(\frac{d_{xy}}{R}\right)^2\right) \tag{3.2}$$

- primary vertex lies outside of the track helix:

$$L_{xy}^{\text{exp}} = \frac{d_{xy}}{\sin\left(\phi_{\text{track}} - \phi_{\text{dijet}}\right)} \left(1 + \frac{d_{xy}}{R}\right) + o\left(\left(\frac{d_{xy}}{R}\right)^2\right) \tag{3.3}$$

The difference between the two cases above lies only in the sign of the track curvature correction. This sign, however, can be determined from the track charge and the vector product between the track transverse momentum vector and transverse impact parameter vector:

$$q \cdot sgn\left(\left(\vec{d_{xy}} \times \vec{p_T}\right) \cdot \vec{z}\right) \tag{3.4}$$

where $\vec{z}$ is a unit longitudinal vector. The final formula applied to each track is thus:

$$L_{xy}^{\text{exp}} = \frac{d_{xy}}{\sin\left(\phi_{\text{track}} - \phi_{\text{dijet}}\right)} \left(1 + q \cdot sgn\left(\left(\vec{d_{xy}} \times \vec{p_T}\right) \cdot \vec{z}\right) \cdot \frac{d_{xy}}{R}\right) \tag{3.5}$$

For a genuine secondary vertex associated with a dijet pair the $L_{xy}^{\text{exp}}$ values obtained with Eq. 3.5 for each track should be close together, therefore we perform a one-dimensional hierarchical clustering algorithm (Appendix A) in order to select tracks belonging to the cluster. Clustering is performed with a size parameter equal to 15% of the vertex $L_{xy}$ reconstructed with the vertex fitter. The tracks are added to the cluster in cases where the distances between the $L_{xy}^{exp}$ values are not larger than the size parameter. If two or

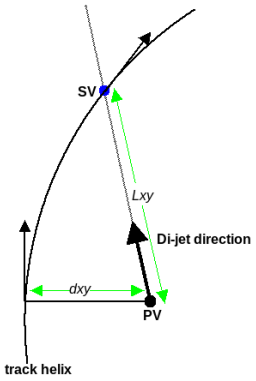


Figure 3.7: Graphical representation of the crossing point (SV) between track helix and a straight line originating from the primary vertex (PV) in the direction of the dijet momentum.

more clusters are reconstructed, the one closest to the vertex is selected. This algorithm is complementary to the vertex fitter since it uses additional information about the dijet direction. Discriminating variables provided by this algorithm include:

- cluster track multiplicity, Fig. 3.8;
- cluster RMS - a root-mean-square of the $L_{xy}^{\exp}$ values belonging to the cluster relative to the vertex $L_{xy}$ given by Eq. 3.6. In addition to cluster density, this variable provides information on whether both vertex and cluster reconstructions share the same tracks. If the two sets of tracks are different, the value of the cluster RMS is greatly increased, see Fig. 3.8.

$$\mathrm{RMS}_{\mathrm{cluster}} = \sqrt{1/N_{\mathrm{tracks}} \sum_{i=0}^{N_{\mathrm{tracks}}} \frac{\left(L_{xy}^{\exp}(i) - L_{xy}\right)^2}{L_{xy}^2}} \tag{3.6}$$

## 3.3 Selection

To determine the background level, we use a data-driven technique of independent selection criteria, the "ABCD method", which is described in detail in Section 4.1. This method requires at least two selection criteria where the probability of a background candidate to pass one criterion is not correlated with whether it passes the other criterion. Such selection

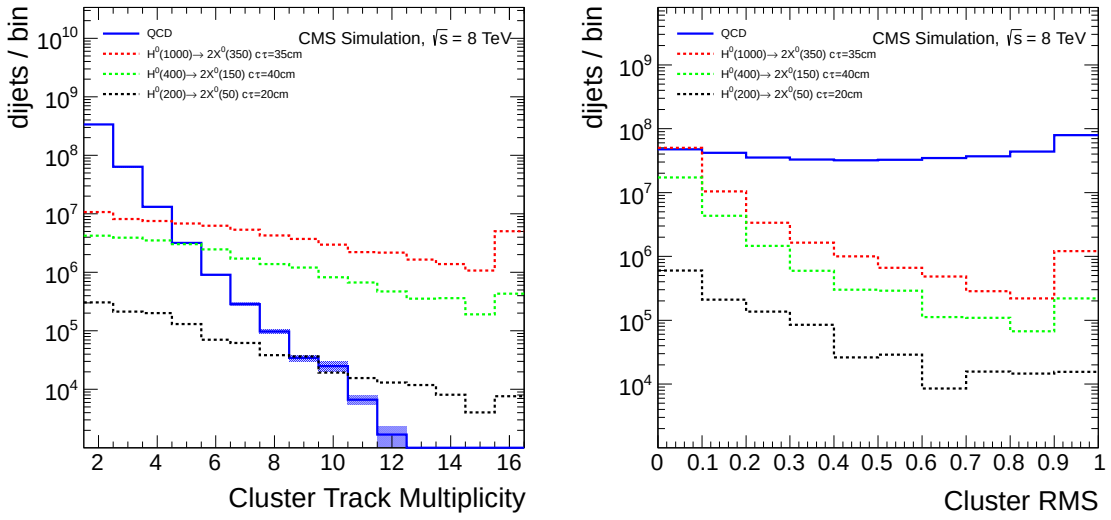


Figure 3.8: Cluster discrimination variables for signal and background MC sample.

criteria generally can be constructed from variables that are mutually independent. In order to eliminate pairs of variables that are not independent, correlation factors have been studied using the background samples. Correlation factors between variables $x$ and $y$ are obtained from binned two-dimensional histograms according to the formula:

$$\mathrm{corr}(x,y) = \mathrm{cov}(x,y)/\mathrm{RMS}(x)\mathrm{RMS}(y), \;\; \mathrm{cov}(x,y) = \sum_i (x_i y_i)/N - \sum_i (x_i)/N \sum_i (y_i)/N \tag{3.7}$$

where N is the normalization of the histogram and the index $i$ loops over the histogram bins. Based on the study of the correlation factors, we construct three independent selection criteria for the background estimation:

1. **Combination of the number of prompt tracks and prompt-track jet-energy-fraction selections** - for first jet in the dijet pair;

2. **Combination of the number of prompt tracks and prompt-track jet-energy-fraction selections** - for second jet in the dijet pair;

3. **Combined vertex and cluster likelihood discriminant**. We select variables that have small signal model dependence and are uncorrelated with prompt tracks variables. They include:

- vertex track multiplicity;
- fraction of tracks assigned to the vertex with positive value of signed transverse impact parameter;
- cluster track multiplicity;
- cluster RMS.

The likelihood discriminant is obtained using signal and background MC samples, where samples for various signal models are added together due to the small signal dependence of the variables used. For each dijet candidate a signal probability is computed according to the formula:

$$p = \frac{p_S}{p_S + p_B} = \frac{1}{1 + p_B/p_S} = \frac{1}{1 + \Pi_i p_{Bi}/p_{Si}} \tag{3.8}$$

where the index $i$ loops over variables included in the discriminant. The correlations between individual variables within the discriminant are neglected. Individual probability densities are determined using one-dimensional histograms for signal and background candidates separately.

As presented in Table 3.1, the individual correlation factors between the variables used for background estimation do not exceed the few-percent level in the background MC samples. There are large correlations between the number of prompt tracks and jet energy fraction carried by prompt tracks for the same jet, hence these two selections are applied together, while there is very little correlation for these variables between the two jets that form the dijet pair. The choice of variables is motivated by the independence of the prompt track variables between the two jets, while the variables associated with the secondary vertex use displaced tracks from both jets simultaneously.

The final numerical values required for the variables used for background estimation are described in Section 4.2. For all remaining discrimination variables we require loose preselection criteria:

- vertex mass $> 4\,\mathrm{GeV}$;

Table 3.1: Correlation factors obtained with Eq. 3.7 between the variables used for background estimation obtained from background QCD MC samples. N1 and N2 represent the numbers of prompt tracks for jets 1 and 2, respectively, while fraction 1 and fraction 2 represent the jet energy fraction carried by prompt tracks.

| | Vtx/Cluster | N1 | N2 | fraction 1 | fraction 2 |
|---|---|---|---|---|---|
| Vtx/Cluster | - | 1.1% | 2.5% | -2.7% | 1.8% |
| N1 | | - | 2.3% | 26% | 1.2% |
| N2 | | | - | 0.5% | 31% |
| fraction 1 | | | | - | 0.3% |
| fraction 2 | | | | | - |

- vertex $p_T > 8\,\text{GeV}$;
- $L_{xy}$ significance $> 8$;
- average number of missing tracker hits after the secondary vertex position $\leq 2$ per track.

The reconstruction and preselection procedure may result in multiple candidates per event that all pass the preselection criteria. In such cases, we select only one candidate per event by choosing the one with the highest number of tracks associated with the secondary vertex. If two or more candidates have the same number of tracks associated with the secondary vertex, we choose the candidate with a smaller $\chi^2$/dof. The candidate preselection together with the selection of the single candidate per event will be further referred to as event preselection. Only the properties of the one selected candidate are used for further selection and background estimation. More than 99% of the background MC events contain only one candidate after the preselection criteria are applied.

Preselection criteria efficiencies are presented in Table 3.2. When the preselection requirements are applied to each dijet candidate, the efficiencies are computed using the number of events with at least one candidate fulfilling the selection. The requirement for the signal candidates to be matched with a decay of an $X^0$ boson at the generator level, denoted in Table 3.2 as *signal dijet*, is inefficient with respect to the trigger, if the two triggering jets do not originate from the same $X^0$ boson particle. The $H_T > 300\,\text{GeV}$ requirement imposed by the trigger reduces the efficiency for lower masses of the $H^0$, while

the vertex reconstruction efficiency is affected by the acceptance of the CMS tracker, which cannot reconstruct vertices displaced by more than 60 cm in the transverse plane. However, if the trigger accepted a signal event and the secondary vertex is reconstructed for at least one of the $X^0$ boson candidates the preselection efficiency is high for the signal samples when compared to the background.

Table 3.2: Trigger and preselection criteria efficiency for data, background MC, and three selected signal models. Event selection efficiencies in each row are relative to events that passed the criteria from rows above. All criteria, except the trigger, are applied to individual dijet candidates. There may be many dijet candidates in a single event, therefore for those criteria the efficiency is computed using the number of events containing at least one dijet candidate that fulfills the selection.

| | preselection criteria efficiency | | | | |
|---|---|---|---|---|---|
| selection | data | bkg. MC | $M_H$=1000 GeV $M_X$=350 GeV $c\tau$=35 cm | $M_H$=400 GeV $M_X$=150 GeV $c\tau$=40 cm | $M_H$=200 GeV $M_X$=50 GeV $c\tau$=7 cm |
| trigger | - | 0.01% | 97% | 53% | 3.9% |
| has dijet | 99% | 99% | 100% | 100% | 99% |
| signal dijet | - | - | 88% | 65% | 21% |
| has vertex | 25% | 24% | 69% | 59% | 61% |
| has cluster | 72% | 72% | 99% | 98% | 98% |
| vertex $\chi^2$ | 93% | 93% | 100% | 99% | 99% |
| vertex mass | 78% | 82% | 98% | 97% | 74% |
| vertex $p_T$ | 43% | 42% | 97% | 95% | 92% |
| max missing hits | 8.5% | 12% | 98% | 98% | 98% |
| $L_{xy}$ significance | 78% | 68% | 100% | 100% | 100% |

In order to validate the simulation based study, we compare the data and background MC distributions in a control region for events passing the preselection. We use a control region that requires passing the single jet trigger and vetoes events passing the double jet trigger (the single and double jet trigger definitions are given in Section 2.3.1). Compared to the signal region, there is a factor of 100 less integrated luminosity and the signal efficiency for all considered signal models is at least ten times smaller than the efficiency in the signal region. Figs. 3.9 through 3.12 present all of the discrimination variables used in the analysis in the control region after event preselection. The number of missing hits per track after the vertex requirement has been removed in order to increase the statistics of

the data and background MC samples. Good agreement between data and background MC is found in most of the cases, suggesting that background sources are well modeled in the MC simulation.

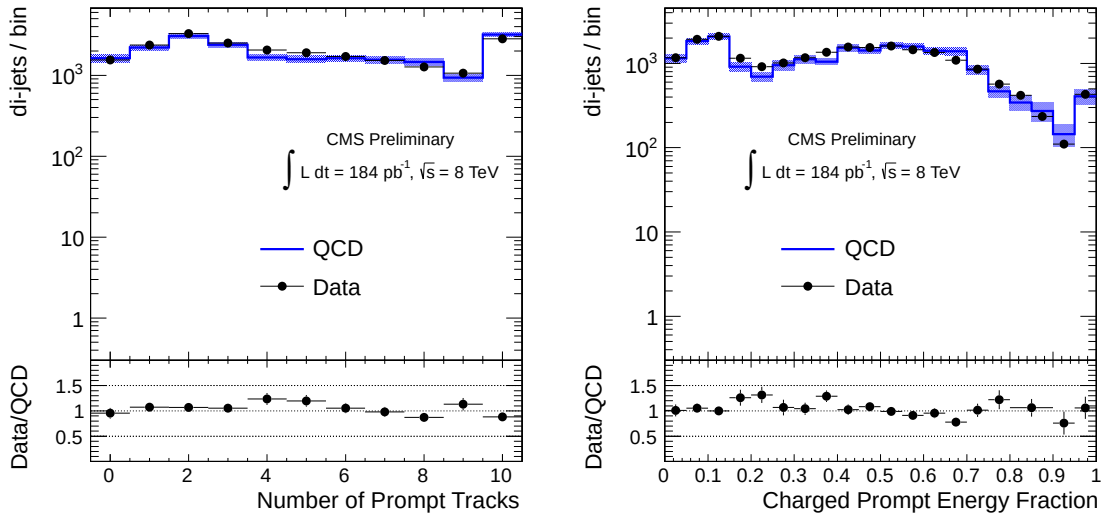


Figure 3.9: Prompt track variables corresponding to the ones used in the trigger. The characteristic shape towards low values in both variables shows the contribution of jets passing the non-prompt trigger requirement.

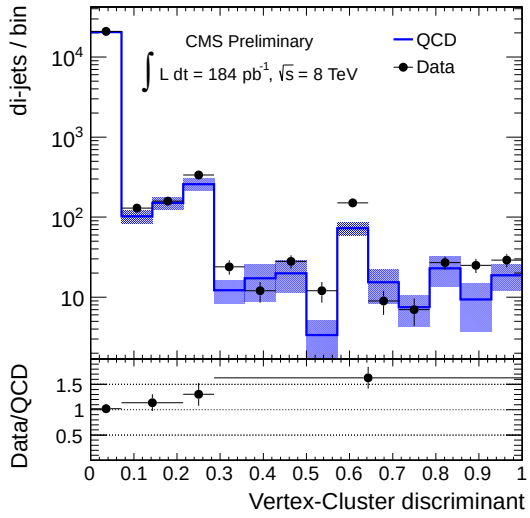


Figure 3.10: Vertex-Cluster likelihood discriminant.

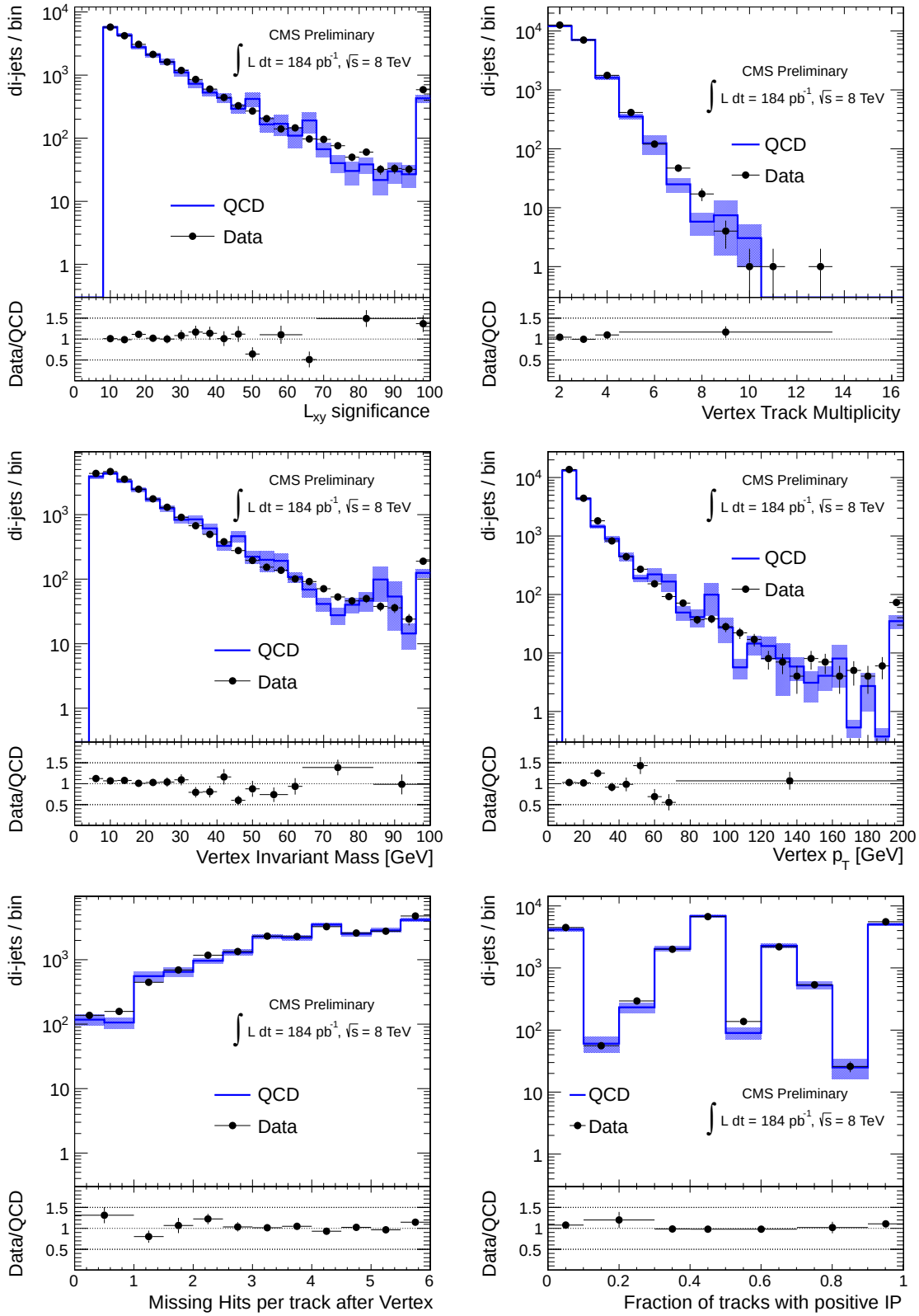


Figure 3.11: Vertex variables.

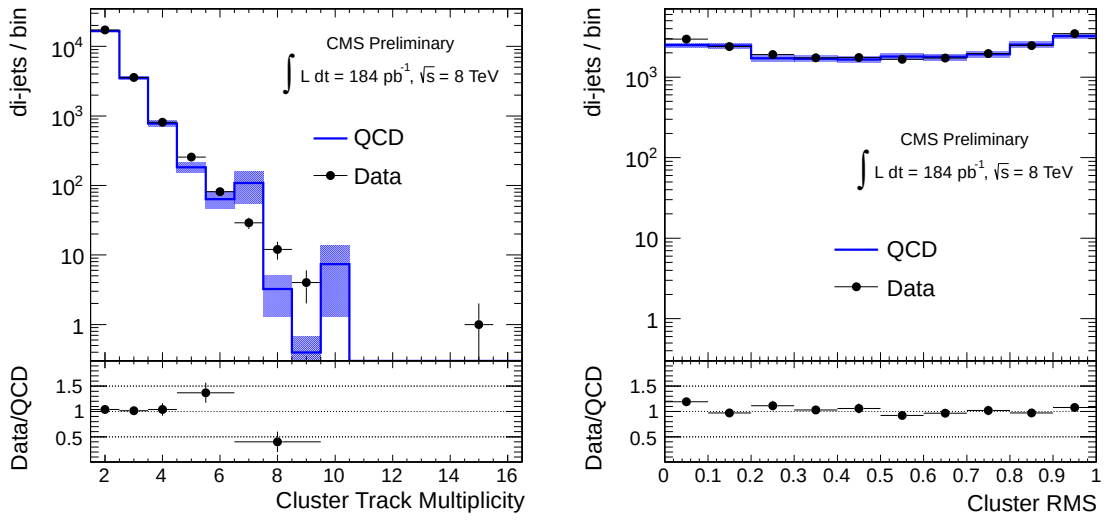


Figure 3.12: Cluster of $L_{xy}^{\text{exp}}$ variables. Candidates for which cluster RMS is above 1 do not share tracks between the vertex and cluster reconstructions.

# Chapter 4

# Background

This chapter focuses on a precise estimate of the search background. The background prediction is of crucial importance for searches beyond the SM because an observation of an upward deviation with respect to the background prediction may hint at a new discovery. First, a data-driven background estimate is introduced. The benefit of a data-driven technique as compared to a simulation-based estimate is that it avoids possible issues of mismodelling. Finally, tests of the background estimate are performed in control regions to establish the correctness of the method and to assess its systematic uncertainty.

## 4.1 Method of uncorrelated variables (ABCD)

We use a data-driven method of independent selections, "the ABCD method". To establish the notation, we introduce a simple version of the method that involves two independent selection criteria. As schematically presented in Fig. 4.1 with two selection criteria one can divide the events into four regions. The regions A, B, and C are background dominated because the events that fall into those regions fail at least one of the selection criteria which have been optimized for signal detection. Given that for background events the probability of passing the first criterion is independent from whether it passes the second criterion, the number of background events in the signal region, D, can be obtained from the event counts

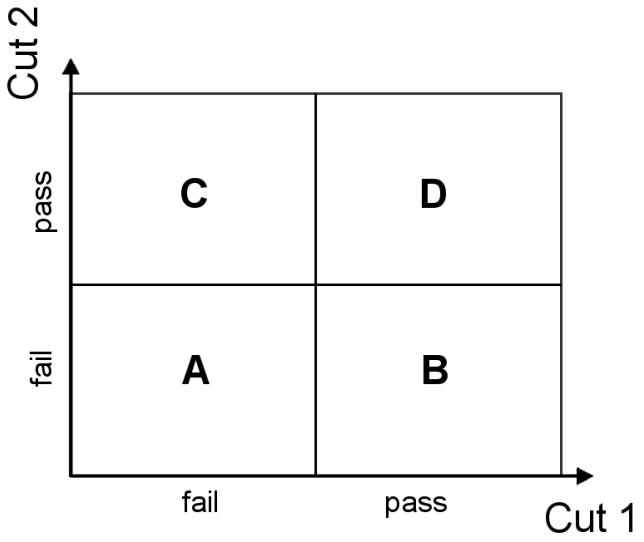


Figure 4.1: Naming convention for the regions used in "the ABCD method".

in regions A, B and C using the formula:

$$\mathrm{D} = \frac{\mathrm{BC}}{\mathrm{A}} \tag{4.1}$$

In this analysis, we use an extension of "the ABCD method" using three, instead of two, independent selection criteria, see Section 3.3 for the definitions of those criteria for displaced dijets. The three selection criteria divide the events into eight regions (A, B, C, ..., H), as listed in Table 4.1, with H being the signal region.

Table 4.1: Naming convention for the regions used in background estimation. "+" corresponds to a selection being applied, while "–" to a selection being inverted.

| Region | selection 1 | selection 2 | selection 3 |
|---|---|---|---|
| A | – | – | – |
| B | + | – | – |
| C | – | + | – |
| D | – | – | + |
| E | – | + | + |
| F | + | – | + |
| G | + | + | – |
| H | + | + | + |

With three independent selections the background level in the signal region H can be

estimated from various combinations of the event counts in other regions. Among the suitable combinations there are six that use event counts in only three regions, namely:

1. FG/B = (+,–,+)(+,+,–) / (+,–,–) – the right hand side of the equation uses a notation that indicates which selections are passed and which are failed by the events in a given region i.e. (+,–,+) corresponds to region F where events pass the first and third selection, while they fail the second selection;

2. EG/C = (–,+,+)(+,+,–) / (–,+,–)

3. EF/D = (–,+,+)(+,–,+) / (–,–,+)

4. DG/A = (–,–,+)(+,+,–) / (–,–,–)

5. BE/A = (+,–,–)(–,+,+) / (–,–,–)

6. CF/A = (–,+,–)(+,–,+) / (–,–,–)

A seventh background prediction can be formed by combining three of the predictions above:

$$\frac{\mathrm{DG/A} \cdot \mathrm{BE/A}}{\mathrm{EG/C}} = \frac{\mathrm{BCD}}{\mathrm{A}^2} = \frac{(+,-,-)(-,+,-)(-,-,+)}{(-,-,-)^2} \tag{4.2}$$

The combination $\mathrm{BCD/A}^2$ is constructed from regions with at least two selections inverted. It minimizes the statistical uncertainty on the background estimate, because in regions A, B, C, and D the background event counts are largest. We use $\mathrm{BCD/A}^2$ as our background prediction central value. In the case of perfectly independent variables, all of the combinations above predict statistically consistent amounts of background. However, to account for possible systematic effects due to residual dependence of the selections, we assign a systematic uncertainty that is equal to the largest difference between $\mathrm{BCD/A}^2$ and any of the six other predictions.

## 4.2 Selection optimisation

We determine the numerical values of the selection criteria that are employed in the background estimation procedure by optimizing the expected limit for each tested signal model. The signal models considered include various values of the $H^0$ mass, the $X^0$ mass, and the $X^0$ lifetime. The selection variables do not strongly depend on the particles masses, therefore the optimal selection criteria vary only as a function of the mean transverse decay length ($L_{xy}$) of the $X^0$ bosons. We use two sets of selection criteria, depending on whether the mean $L_{xy}$ of the $X^0$ bosons is below or above 30 cm. The selection criteria are detailed in Table 4.2.

Table 4.2: Optimised selection criteria and the corresponding background expectations with their statistical and systematic uncertainties.

| $\mathbf{L_{xy}}$ **selection** | $<$ **30 cm(low)** | $>$ **30 cm(high)** |
|---|---|---|
| prompt tracks | $\leq 1$ | $\leq 1$ |
| prompt energy | $< 0.15\%$ | $< 0.09\%$ |
| vertex/cluster disc. | $> 0.9$ | $> 0.8$ |
| **expected bkg.** | $\mathbf{1.60 \pm 0.26(stat) \pm 0.51(syst)}$ | $\mathbf{1.14 \pm 0.15(stat) \pm 0.52(syst)}$ |

## 4.3 Background tests

The background estimation procedure described in Section 4.1 is general and can be applied to any dataset if the selections used are independent. In this section we describe various background closure tests performed in QCD MC simulation and selected control regions in data. We test the optimal selection criteria from Section 4.2 and also other various selections points. The figures shown in the following sections present the observed number of events along with the seven background estimates which were described in Section 4.1. Uncertainties are statistical only. For each of the tested selection points the background prediction and its uncertainty are obtained using the prescription from Section 4.1. The compatibility between the predicted and observed background is estimated with a *p-value* for each measurement. The *p-value* is computed with respect to the estimated background

probability density function (p.d.f.). The background prediction has an associated uncertainty, therefore the background p.d.f. is a Poissonian function convolved with a Gaussian error function. The probability of observing $n$ background events is given by:

$$B(n, b, \sigma_b) = \frac{1}{\sqrt{2\pi}\sigma_b} \int_0^\infty \exp\left[-\frac{(x-b)^2}{2\sigma_b^2}\right] \frac{x^n e^{-x}}{n!} dx \tag{4.3}$$

where $b$ is the background central value and $\sigma_b$ is the total uncertainty. The Gaussian probability density of the background mean has been truncated at 0 in order to avoid unphysical values. Such a truncation results in a not properly normalized p.d.f. in Eq. 4.3, however the *p-values* computed according to Eq. 4.4 take the normalization into account.

$$p(n_{\text{obs}}, b, \sigma_b) = \sum_{k \geq n_{obs}} B(k, b, \sigma_b) / \sum_k B(k, b, \sigma_b) \tag{4.4}$$

The *p-values* are then converted into *significances* using the normal distribution. The *significances* are shown in the bottom plots (Figs. 4.2-4.4) aligned to the corresponding background measurements.

### 4.3.1 QCD MC background prediction

Due to the limited statistics of the QCD MC samples, the displaced jet trigger requirement has been removed. In addition, the background is estimated with looser selection on prompt tracks variables compared to the final selection. In order to validate the background prediction with the observed Poissonian event counts, the cross-section weights (Table 2.3) are removed. Therefore this test serves only to identify biases due to non-independent selections, and cannot be translated into a background prediction in data. As shown in Fig. 4.2 good agreement between predicted and observed background level is found, and the discrepancy is not significant for the tested selection points. Therefore, we conclude that the bias due to possible interdependence between the variables is small in the QCD MC samples.

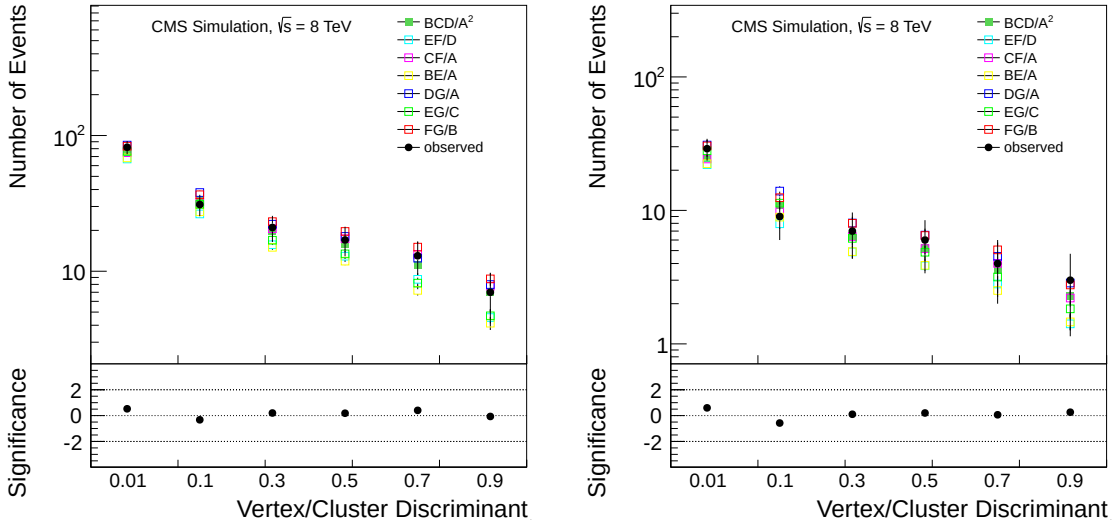


Figure 4.2: Predicted and observed background levels for the QCD MC sample as a function of the vertex discriminant selection criteria. The selection requires at most 5 (left) and 4 (right) prompt tracks and that their jet energy fraction be below 30% (left) and 25% (right), which is significantly looser than the final selection.

### 4.3.2 Data control region

As a data control region we use candidates passing all of the preselection criteria listed in Section 3.3, but with the *missing hits* selection inverted. We again choose only one candidate per event, applying the same procedure as described in Section 3.3. Such a region has a very small signal acceptance compared to the signal region, as the *missing hits* criterion has a very high signal efficiency, while providing a background sample with good statistics. Using this control region we are able to test final selection criteria with amounts and uncertainties of predicted background comparable to the signal region. As shown in Fig. 4.3, the background predictions in this control region are in good agreement with the observed background levels. Given that the significance of the discrepancies is small, we conclude that the background estimation method is valid and the systematic uncertainty on the background prediction is not underestimated.

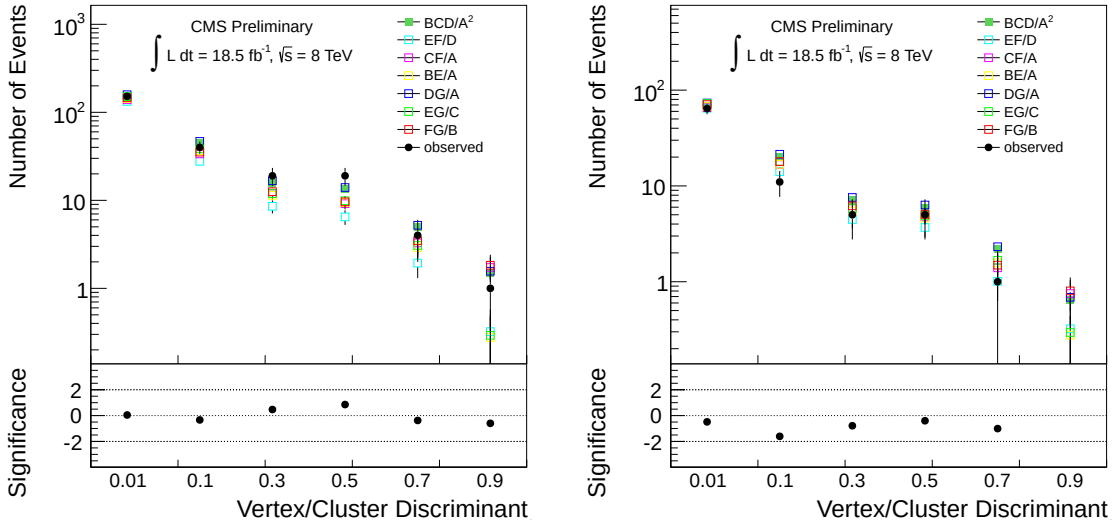


Figure 4.3: Predicted and observed background levels in the data control region as a function of the vertex discriminant selection criteria. The selection requires at most one prompt track and that the jet energy fraction carried by prompt tracks is below 15% and 9% on the left and right plot, respectively.

## 4.4 Background estimate based on 10% of the dataset

In order to check that there is no anomalous background present, we initially examined the data corresponding to only 10% of all available data in the signal region. We select the data using one out of every ten luminosity sections, where a luminosity section is a period of approximately 23 seconds of active data taking. This way of choosing the data is sensitive to possible problems that occur only for selected data taking periods, and also to effects that may arise from correlations between consecutive events accepted by the trigger. A comparison of the data and predicted background is presented in Fig. 4.4. No anomalous background is observed in this sample, however, the background predictions are small, thus limiting the statistical power of the test.

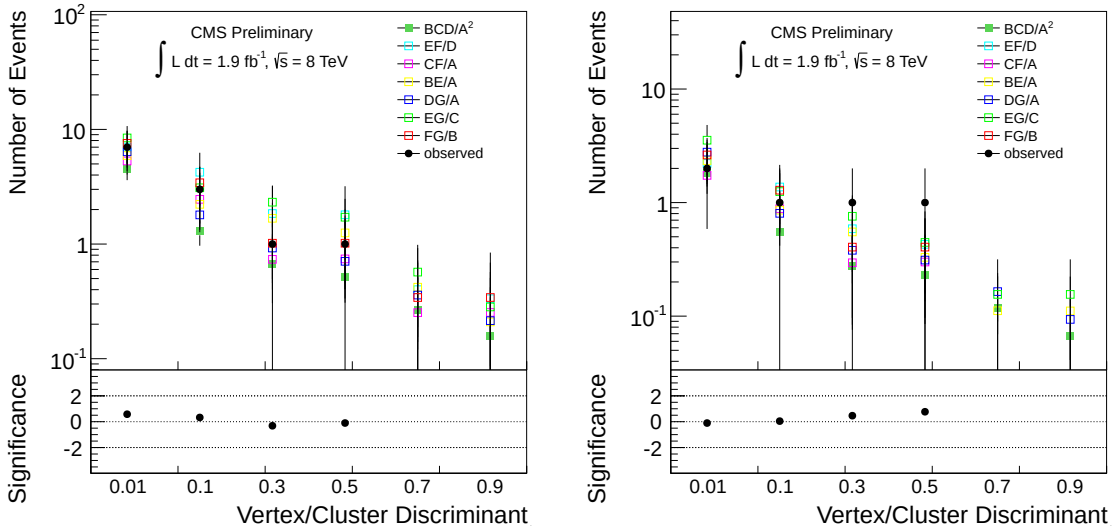


Figure 4.4: Data and predicted background level in the 10% data sample as a function of vertex discriminant selection criteria. The selection requires at most 2 (left) or 1 (right) prompt tracks while the jet energy fraction carried by the prompt tracks is required to be less than 11%.

# Chapter 5

# Systematic Uncertainties

We describe the sources of systematic uncertainty, which include those related to the background prediction, the integrated luminosity, and the signal reconstruction efficiency. The signal efficiencies are obtained from MC simulations of the various signals processed through the full detector simulation. The systematic uncertainties are then estimated by determining the relevant differences between data and simulation using control samples. The sources of systematic uncertainty are discussed below and their impact on the analysis result is evaluated.

As discussed in Section 4.2 the analysis aims to optimize the expected limit on possible signals in data. As shown in Appendix B, an increase in the signal efficiency systematic uncertainty results only in slow degradation in the expected limit. Therefore, when evaluating MC related systematic effects we take a conservative approach.

## 5.1 Background

The systematic uncertainty on the estimated background depends on the final selection used. Using the prescription from Section 4.1 the systematic uncertainty is evaluated to be 32% and 46% for the *low* and *high* $L_{xy}$ selections, with 1.60 and 1.14 predicted background events respectively. The seven background predictions from which the systematic uncertainty is derived are listed in Table 5.1.

Table 5.1: Predicted background level for the final selections obtained with seven combinations using the method of independent selections.

| Selection | low $L_{xy}$ | high $L_{xy}$ |
|---|---|---|
| BCD/A$^2$ | 1.60 | 1.14 |
| FG/B | 1.21 | 1.00 |
| EG/C | 1.92 | 0.84 |
| DG/A | 1.76 | 1.25 |
| BE/A | 1.72 | 0.77 |
| CF/A | 1.08 | 0.92 |
| EF/D | 1.16 | 0.62 |

## 5.2 Luminosity

For the running period corresponding to this analysis, CMS estimates the relative uncertainty on the luminosity to be 2.6% [47].

## 5.3 Effect of Pileup

The likelihood of a given number of pileup events occurring in the data can be calculated from the distribution of the instantaneous luminosity during the 2012 LHC run. The number of true pileup events in the MC simulation is also known. The simulation can therefore be reweighted to match the data.

The systematic uncertainty in this procedure is estimated by adjusting the reweighting, so as to account for uncertainties related to pileup modeling. The effect of a $\pm 5\%$ variation in the number of interactions is estimated and gives rise to a relative systematic uncertainty in the signal reconstruction efficiency of less than 2% for all mass and lifetime points considered. The signal reconstruction efficiency as a function of the number of primary pileup vertices is shown in Fig. 5.1. No significant decrease in efficiency is observed as the number of primary pileup vertices increases.

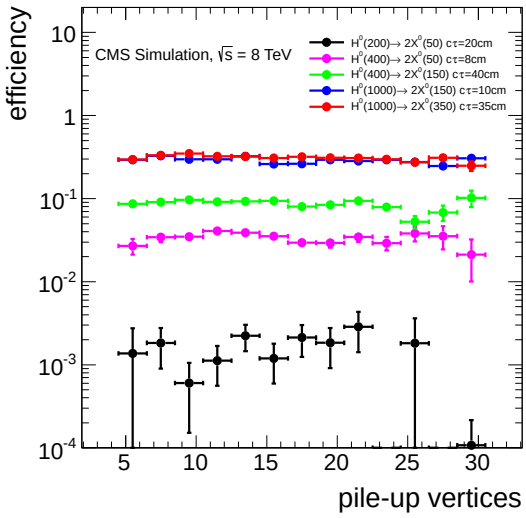


Figure 5.1: Reconstruction efficiency as a function of number of pileup vertices for selected signal models.

## 5.4 Primary vertex selection

The relevant impact parameters and decay lengths are computed with respect to the primary vertex that has the highest squared transverse momentum sum of the tracks. If a dijet candidate does not originate from this vertex the impact parameters would be computed incorrectly. The size of the luminous region, where the primary vertices lie, is $\sim$5 cm in the longitudinal direction and $\sim$15$\mu$m in both transverse directions. Therefore the effect of an incorrect primary vertex assignment significantly increases the 3-D impact parameters, while for the transverse impact parameters the effect is small, as the size of the luminous region is smaller than the primary vertex resolution (20$\mu$m). In the displaced dijet selection criteria the 3-D impact parameters are used to compute the number of jet prompt tracks, while all other criteria employ only the transverse impact parameters. We study the background levels and signal reconstruction efficiency where all the relevant impact parameters and decay lengths are computed with respect to the second, instead of the first, primary vertex. In this scenario the selection of an incorrect primary vertex is greatly enhanced. The predicted and observed background level are detailed in Table 5.2.

The predicted background level increases by a negligible amount if a wrong primary

Table 5.2: Predicted and observed background for the optimised selections for first and second highest squared transverse momentum sum primary vertex in the event. Uncertainties on the background level include both statistical and systematic uncertainties.

| | low $L_{xy}$ ($1^{st}$ PV) | low $L_{xy}$ ($2^{nd}$ PV) |
|---|---|---|
| predicted bkg. | $1.60 \pm 0.57$ | $1.67 \pm 0.75$ |
| observed bkg. | 2 | 2 |

| | high $L_{xy}$ ($1^{st}$ PV) | high $L_{xy}$ ($2^{nd}$ PV) |
|---|---|---|
| predicted bkg. | $1.14 \pm 0.54$ | $1.17 \pm 0.66$ |
| observed bkg. | 1 | 1 |

vertex is used. The signal reconstruction efficiency does not significantly change whether the first or second leading primary vertex is used.

## 5.5 Displaced Tracking Efficiency

The signal reconstruction efficiency is obtained assuming the tracking efficiency is correctly accounted for in the MC simulation. In order to validate this assumption we study the relative tracking efficiency as a function of displacement and pileup using $\mathrm{K}^0_\mathrm{S} \to \pi^+\pi^-$ decays in data and simulation. The $\mathrm{K}^0_\mathrm{S} \to \pi^+\pi^-$ decay mode, with the $\mathrm{K}^0_\mathrm{S}$ proper decay length of 2.68 cm [48], provides an abundant source of tracks originating at displaced locations. The tracking efficiency for $\mathrm{K}^0_\mathrm{S}$ pions can be used to check the displaced jet tracking efficiency, as the jet tracks consist mostly of low-momentum light hadrons.

### 5.5.1 Displaced pion tracking efficiency

Data and simulation events are selected with the multijet trigger, thus providing a source of $\mathrm{K}^0_\mathrm{S}$ decays in a jet environment. The pileup distribution in simulation is reweighted to match the corresponding distribution in data. To obtain a clean sample of $\mathrm{K}^0_\mathrm{S}$ mesons, pairs of tracks with $p_T > 1\,\mathrm{GeV}$ are combined into a secondary vertex with the following criteria:

- secondary vertex $\chi^2$/degree of freedom $< 7$
- decay length significance of the secondary vertex $> 5$

- significance of the three-dimensional impact parameters for both pion tracks $> 3$
- significance of the three-dimensional impact parameter of the $K^0_S$ candidate $< 3$

where the decay lengths and impact parameters are computed with respect to the leading primary vertex in the event. The invariant mass of the secondary vertex distribution is shown in Fig. 5.2. In Fig. 5.2, as well as all other figures presented in this section, in order to reduce the effect of statistical fluctuations, the data/simulation ratio histograms are shown with neighbouring bins merged until the relative statistical uncertainty does not exceed 2%.

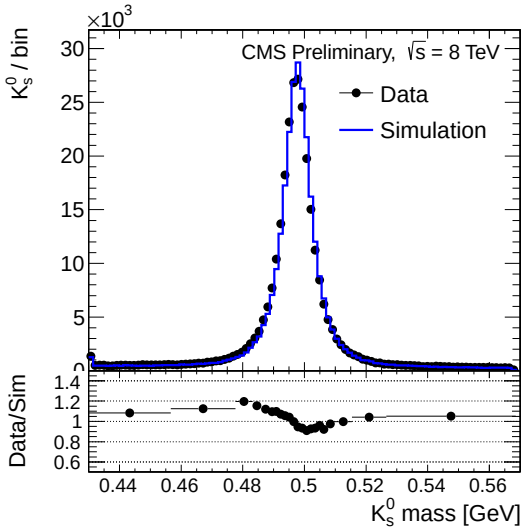


Figure 5.2: Invariant mass distribution of the $K^0_S$ candidates in data and simulation.

The mean lifetime of the $K^0_S$ is known with better than 0.1% precision, however the $K^0_S$ production rate as well as its kinematic distributions are not perfectly reproduced by PYTHIA [49]. In order to remove a potential bias arising from the generator level discrepancies, we select the $K^0_S$ candidates with transverse decay length $L_{xy} < 2\,\text{cm}$, where tracking efficiency is high and well simulated. We then compare $p_T$ and $\eta$ distributions for these candidates and obtain weights, binned in $p_T$ and $\eta$, as well as an overall scale factor that are further applied for all $K^0_S$ candidates.

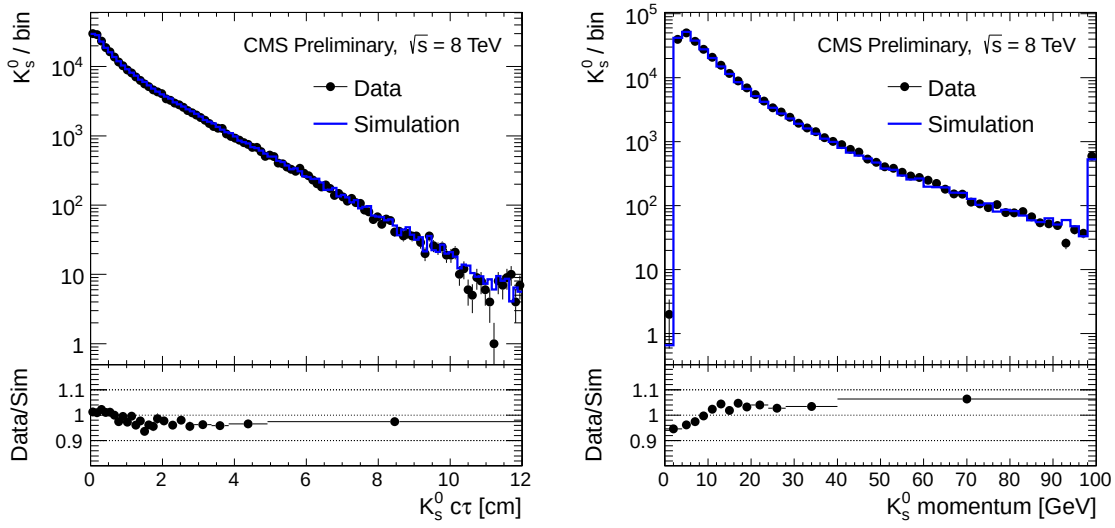


Figure 5.3: Proper lifetime and momentum distributions of the $K^0_S$ candidates in data and simulation.

The proper lifetime and momentum distributions of the $K^0_S$ candidates are shown in Fig. 5.3, while Fig. 5.4 shows the two and three dimensional decay lengths and track impact parameter distributions for data and simulation. Good agreement between data and simulation is found, with simulation deviations not exceeding 10%.

The average number of reconstructed $K^0_S$ candidates as a function of pileup is presented in Fig. 5.5. The tracking efficiency is found to decrease more rapidly in data than simulation, but the overall difference is not bigger than 5%.

The $K^0_S$ reconstruction efficiency is proportional to the single-track reconstruction efficiency squared, therefore the deviations between data and simulation of $K^0_S$ distributions can be translated to deviations in the single track reconstruction efficiency that are half as large. We conservatively adopt the largest deviation of 10% as the systematic uncertainty on the $K^0_S$ efficiency and therefore assign 5% systematic uncertainty on the single track reconstruction efficiency.

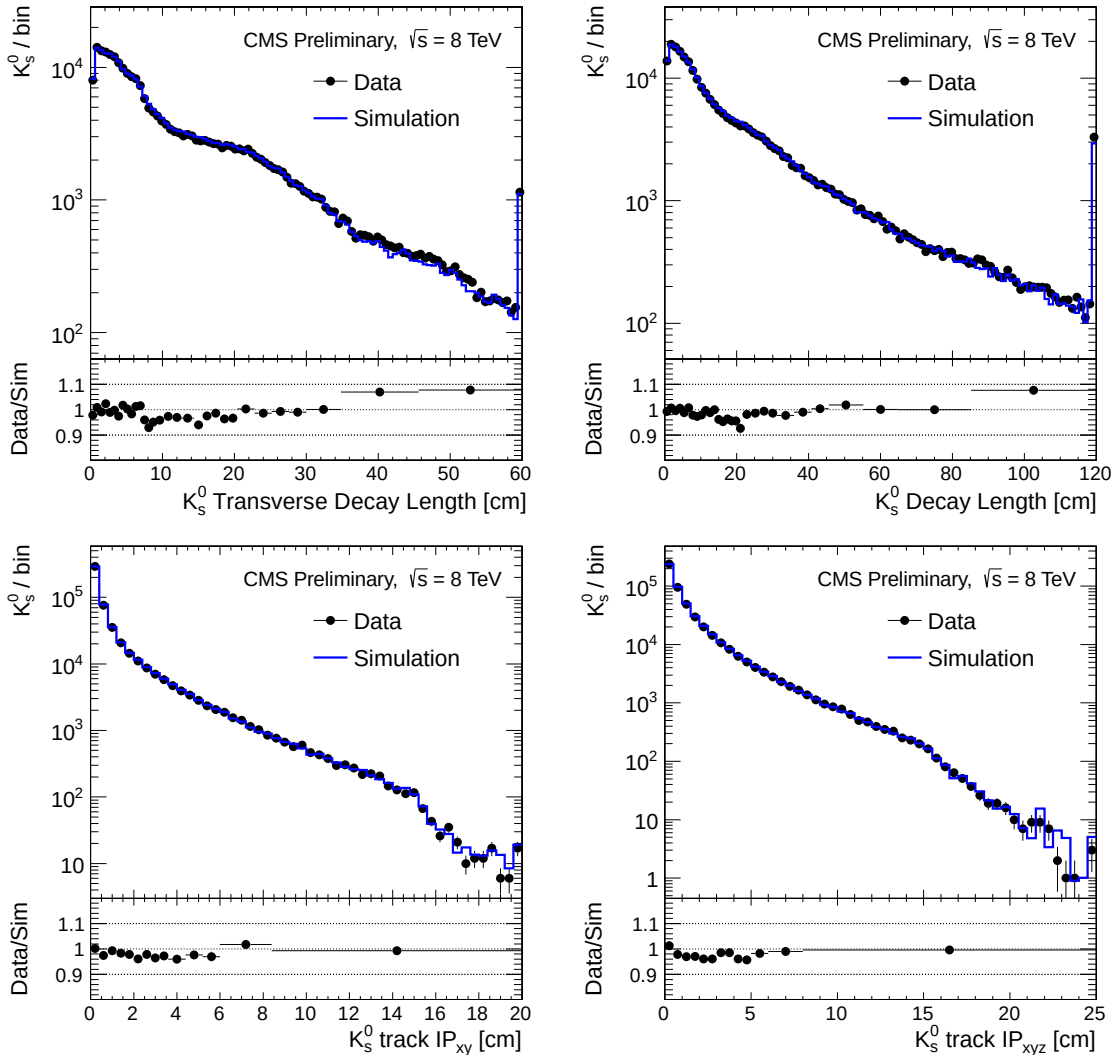


Figure 5.4: Two-dimensional (top-left) decay length, three-dimensional decay length (top-right), two-dimensional track impact parameter (bottom-left) and three-dimensional track impact parameter (bottom-right) distributions of the $K^0_S$ candidates in data and simulation.

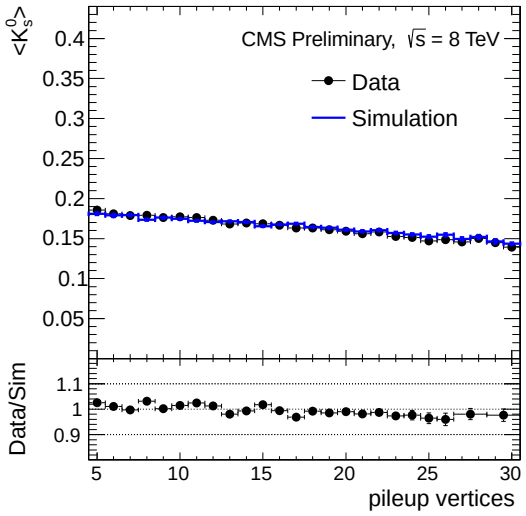


Figure 5.5: Average number of reconstructed $K^0_S$ candidates as a function of the number of primary vertices in data and simulation.

### 5.5.2 Impact on the signal reconstruction efficiency

We examine the effect of the tracking efficiency systematic uncertainty by removing 5% of the displaced tracks and repeating the signal reconstruction procedure. For all signal models the reconstruction efficiency is lowered by up to 4%, which we adopt as our reconstruction efficiency systematic uncertainty from this source.

## 5.6 Missing track hits

In the preselection criteria the tracks in the displaced dijet vertex are required to have on average fewer than two missing hits after the vertex position. The efficiency of this requirement is above 98% for the simulated signal dijets as shown in Table 3.2. The number of missing measurements depends on the number of tracking modules that are capable of providing valid hits along the path of each track. This may not be properly simulated as the overall number of non-functional modules changes over the data taking period. We study the average number of missing hits after the vertex position in a control sample of prompt dijets in data and simulation. We apply the selection criteria that are analogous to the

selection criteria applied to the signal dijets, while omitting the requirements on prompt tracks and vertex displacement. Fig. 5.6 presents the average number of missing hits after the vertex position per track for prompt dijets in data and simulation.

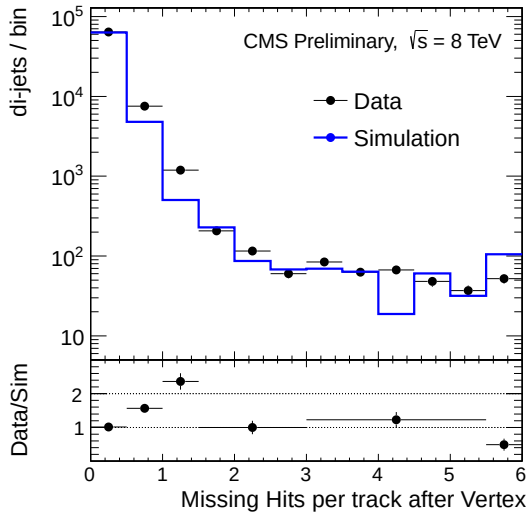


Figure 5.6: Average number of tracker missing hits after vertex position per track for prompt dijets in data and simulation.

There are more missing hits observed in data, however, the requirement of less than two missing hits is on average 98% efficient in both data and simulation. Given the agreement in the efficiency of this selection we do not assign additional systematic uncertainty.

## 5.7 Jet energy scale

In the CMS reconstruction the jet energies are determined by applying a set of corrections. The systematic uncertainties on the corrections are also provided. The uncertainties vary as a function of jet $p_T$ and $\eta$ and are different depending on the jet algorithm [50]. Therefore, the effect of these uncertainties on the signal reconstruction efficiency needs to be evaluated by applying variations to individual jets. In the event selection described in Section 3.3, we use the jet energy information in the following criteria:

- $H_T > 325\,\text{GeV}$– using jets with $p_T > 40\,\text{GeV}$ and $|\eta| < 3$;

- $p_T > 60\,\text{GeV}$ for both jets of the dijet candidate - here jets within $|\eta| < 2$ are used.

We determine the systematic uncertainty due to the jet energy scale by shifting all relevant jet energies by $\pm 1$ standard deviation. The systematic difference in the signal reconstruction efficiency upon jet energy scale variations is presented in Table 5.3. For a $H^0$ mass of 1000 GeV the uncertainty is negligible, while for lower masses of the $H^0$ the systematic effect is below 5%.

Table 5.3: Signal reconstruction efficiency relative bias ($\Delta\epsilon$) due to jet energy scale uncertainties.

| $M_{H^0}$ [ GeV ] | $M_{X^0}$ [ GeV ] | $\Delta\epsilon$ |
|---|---|---|
| 200 | 50 | 4.4% |
| 400 | 50 | 2.7% |
| 400 | 150 | 4.8% |
| 1000 | 150 | 0.03% |
| 1000 | 350 | 0.02% |

## 5.8 Jet momentum bias

$X^0$ boson jets originate at transversely displaced locations, which leads to two effects that are relevant for the jet momentum determination:

- skewed approach angle at the calorimeter's face. This effect is a result of the displacement of the jet production point combined with the opening angle of the $q\overline{q}$ pair. If the angle is large, the jet particles pass sideways through the calorimeters, which results in a geometrical bias of the individual particle's momentum and therefore the entire jet momentum;

- reduced tracking efficiency for tracks originating far from the interaction point. In the jet reconstruction algorithm, when charged particles are not reconstructed as tracks, they are assumed to be neutral particles, therefore the jet charged-energy fraction is underestimated in favor of the neutral-energy fraction. The calorimeter response to charged and neutral particles is different, therefore the mismeasured energy fractions lead to biased jet energy corrections.

Fig. 5.7 shows the bias (points) and the resolution (error bars) of the signal jets' $p_T$ as a function of the $X^0$ boson transverse decay length $L_{xy}$.

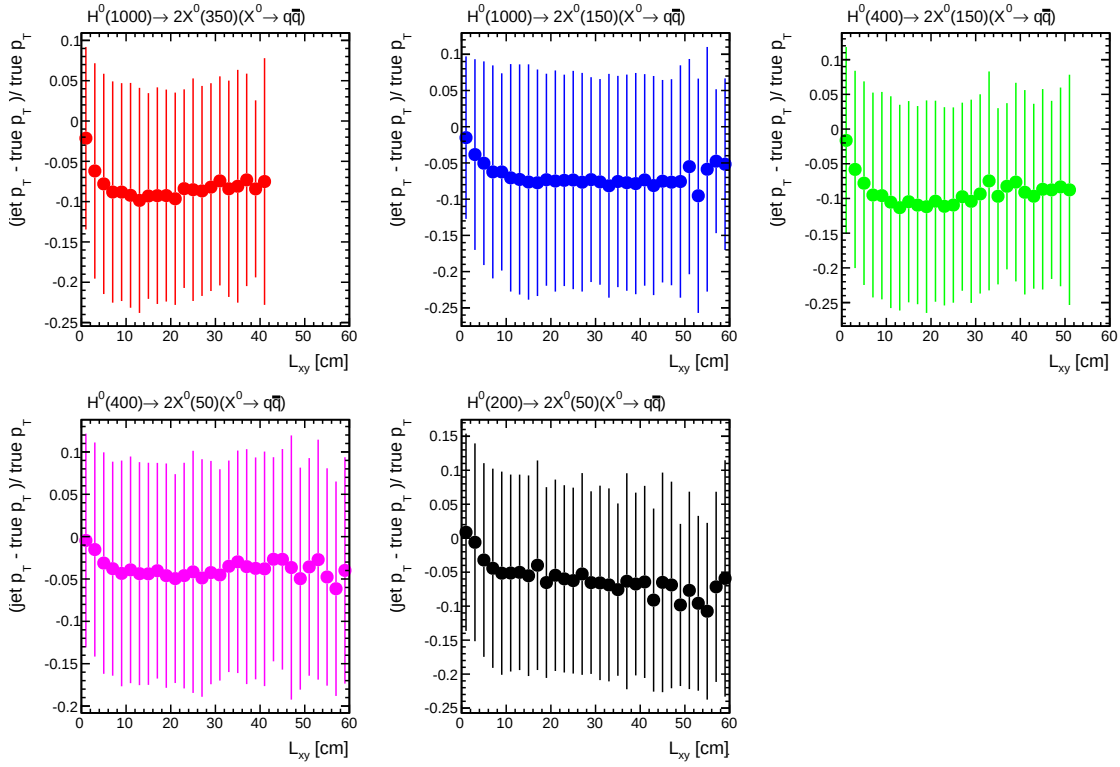


Figure 5.7: Signal jet $p_T$ bias and resolution as a function of the $X^0$ boson transverse decay length.

The jet momentum bias due to geometrical displacement is found to be as large as -10% for dijet candidates with transverse decay lengths below 60 cm, while it is small for the prompt jets as expected. The level of the bias differs depending on the signal mass point chosen, while the variation is related to the calorimeter approach angle, which is influenced by the opening angle of the $q\bar{q}$ pairs. The jet-momentum bias as a function of the calorimeter approach angle is shown in Fig. 5.8. If the jet approach angle is restricted to below one degree, the jet momentum bias is reduced by half. Therefore, the two effects related to tracking efficiency and skewed approach angle contribute to the momentum bias in approximately the same amounts.

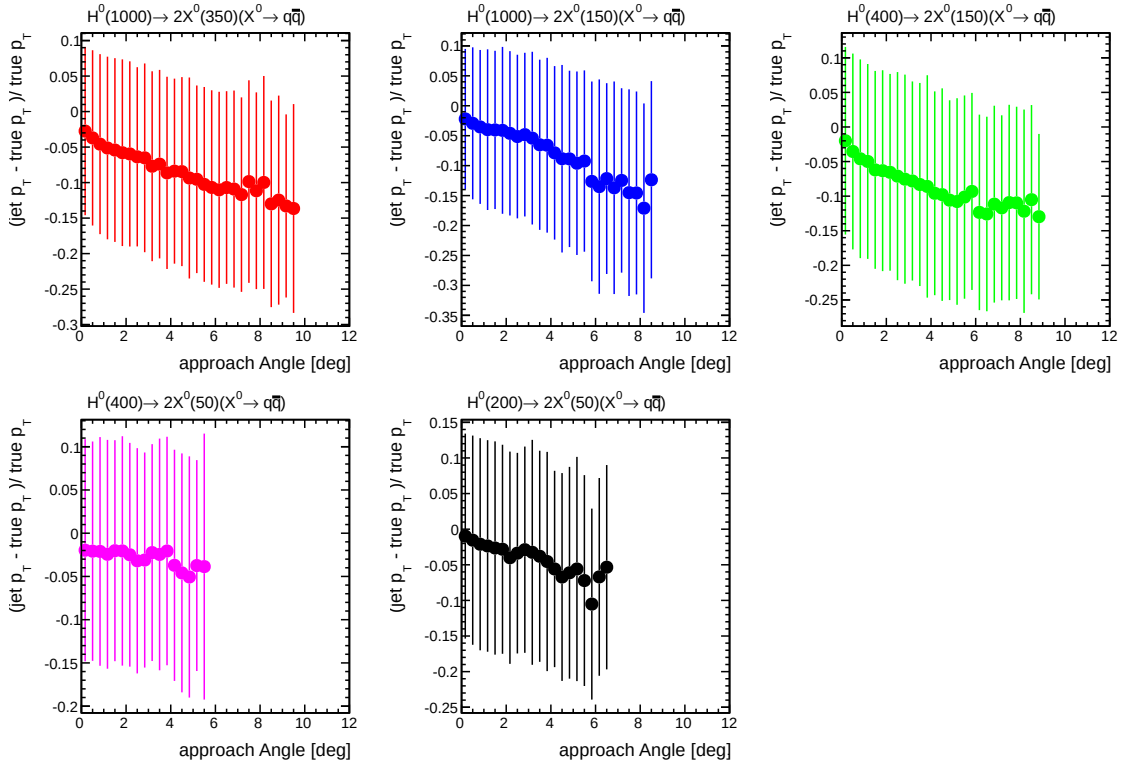


Figure 5.8: Signal jet $p_T$ bias and resolution as a function of the jet approach angle at the calorimeters.

We do not assign a systematic uncertainty related to the jet momentum bias arising from the skewed approach angle at the calorimeters under the assumption that the detector geometry is well described in the MC simulation. In Section 5.5.1 we assign a 5% systematic uncertainty on single-track efficiency for displaced tracks. We therefore study a 5% variation of the jet charged-energy fraction and its impact on the signal reconstruction efficiency with the results presented in Table 5.4.

Table 5.4: Signal reconstruction efficiency bias upon a 5% variation in the jet charged energy fraction.

| $M_{\mathrm{H}^0}$ [ GeV ] | $M_{\mathrm{X}^0}$ [ GeV ] | $\Delta\epsilon$ |
|---|---|---|
| 200 | 50 | 4.9% |
| 400 | 50 | 4.5% |
| 400 | 150 | 3.6% |
| 1000 | 150 | 0.9% |
| 1000 | 350 | 0.5% |

## 5.9 Trigger Efficiency

The double displaced jet trigger, described in Section 2.3.1, has been emulated in all simulation samples. The trigger selection consists of several consecutive filters applied to each event, and the performance of each filter is studied individually in data and simulation with respect to the corresponding offline selection criteria. For studying each individual filter, events passing all trigger decisions are not used in order to avoid a possible bias with the signal sample. Individual filters and their efficiency are described in the following sections.

### 5.9.1 $H_T$ trigger

This trigger filter requires $H_T > 300\,\mathrm{GeV}$. Its performance is studied using a lower threshold trigger that requires $H_T > 250\,\mathrm{GeV}$. The lower threshold trigger was heavily prescaled in 2012 LHC run, therefore the integrated luminosity corresponds to only $8\,\mathrm{pb}^{-1}$. In both trigger calculation and offline reconstruction, hadronic jets with $p_T > 40\,\mathrm{GeV}$ and $|\eta| < 3$ are used for $H_T$ computation. Fig. 5.9 shows the trigger efficiency as a function of the

offline $H_T$. The difference in performance between data and simulation can be inferred from the efficiency ratio shown at the bottom. The observed discrepancy in the turn-on curves close to the threshold is caused by the difference in Level 1 trigger seeds between simulation and data. An offline selection on $H_T$ at 325 GeV is applied. Above this value the differences in efficiency between data and simulation are as large as 7%. To account for these differences the simulation events are reweighted to match the efficiency in data. This reweighting lowers the signal efficiency by up to 2% for all considered signal models. The systematic effects in the turn-on curve shape are studied by reweighting the simulation with data turn-on curves corresponding to different periods of the LHC data taking in 2012. The variations in efficiency are less than 1%, leading us to assign 1% systematic uncertainty corresponding for this trigger filter.

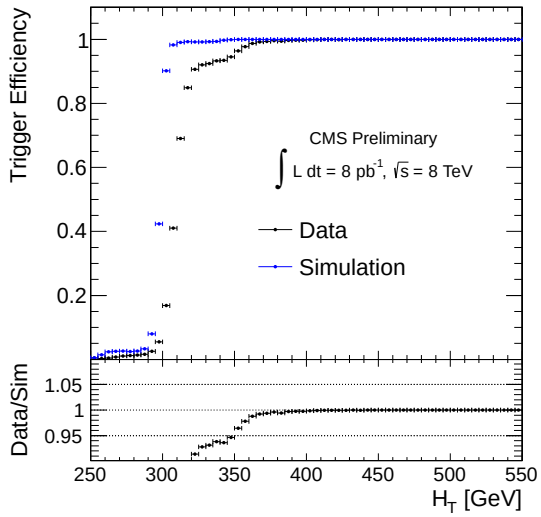


Figure 5.9: $H_T$ >300 GeV trigger efficiency as a function of offline $H_T$ requirement.

### 5.9.2 Two jets, each with no more than two prompt tracks

This filter is analyzed with data passing the previous $H_T$ filter. Data collected by CMS with this filter applied was prescaled and amounts to 17 $\text{pb}^{-1}$. While the filter in question requires at least two jets with $p_T > 60$ GeV passing the requirement, it is sufficient to study only the efficiency of a single jet passing the filter with respect to the number of prompt

tracks computed offline. In both the HLT trigger and the offline reconstruction prompt tracks are selected as those with an impact parameter in three dimensions not bigger than 300 $\mu$m with respect to the leading primary vertex. Fig. 5.10 shows the single jet efficiency for passing the requirement of at most two prompt tracks as a function of the same variable computed offline. The trigger becomes efficient when the number of offline prompt tracks is less than two. A drop in efficiency for the case of zero prompt tracks results from different leading primary vertex assignment between HLT and offline reconstructions. In such a scenario a track may be assumed to be prompt in the HLT and non-prompt in the offline reconstruction or vice versa.

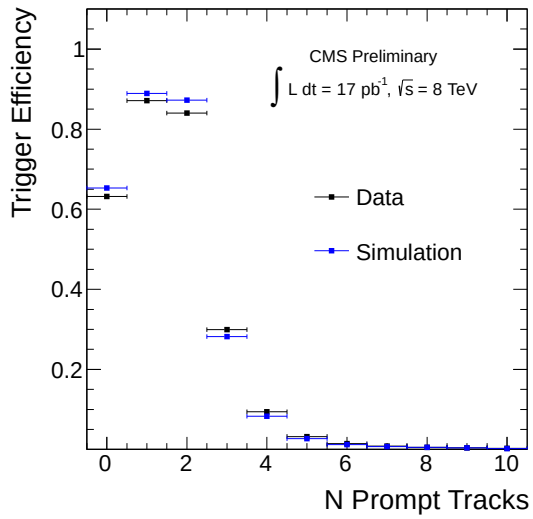


Figure 5.10: Single jet efficiency for jets having maximally of 2 prompt tracks as a function of number of offline prompt tracks.

The trigger efficiency for jets passing the offline selection of at most two prompt tracks is plotted in Fig. 5.11 as a function of $p_T$, $\eta$ and $\phi$. In order to determine the differences in performance between data and simulation the efficiency ratios are fitted with a zeroth order polynomial for each variable. The fits yield ratio values close to 97% for all three functions. This is statistically consistent given the uncertainties in $p_T$, $\eta$ and $\phi$. However, the $\chi^2$ per degree of freedom for the fits is as large as 4. The statistical uncertainties on individual points in the ratio histograms are thus inflated by a factor of 2 and the ratios

refitted. The overall correction is determined from the average of the fit values for $p_T$, $\eta$ and $\phi$ with the result of 97%. The systematic uncertainty on the ratio is assigned as the maximal difference between the fit values within their statistical uncertainties with the result of 0.6%. Therefore, we assign an overall correction of 97% with a conservative 1% systematic uncertainty for each jet passing this trigger filter.

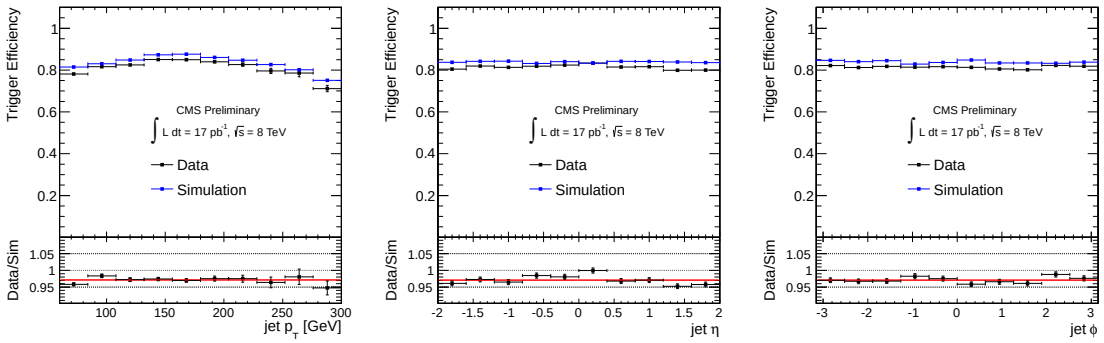


Figure 5.11: Single jet efficiency as a function of jet $p_T$, $\eta$ and $\phi$ for jets with maximally 2 offline prompt tracks.

### 5.9.3 Two jets, each with less than 15% of prompt energy fraction

We require both filters from Sections 5.9.1 and 5.9.2 to accept the event and then examine the single jet efficiency with respect to the prompt charged-energy fraction computed offline. In this trigger step, the prompt tracks are defined as those having a transverse impact parameter smaller than 500 $\mu$m. Using the transverse impact parameter minimizes the sensitivity to additional pileup interactions in the event. The luminous region in the transverse plane is very small, about 15 $\mu$m, therefore the track promptness definition does not depend on the choice of the primary vertex. Trigger efficiency as a function of prompt energy fraction computed offline is shown in Fig. 5.12.

Systematic differences between data and simulation are again studied after an offline requirement that the prompt energy fraction is less than 15%. The efficiency as a function of $p_T$, $\eta$, and $\phi$ is presented in Fig. 5.13. The same procedure used in Section 5.9.2 is followed and the efficiency ratios are fitted with a zeroth order polynomial. No error inflation is

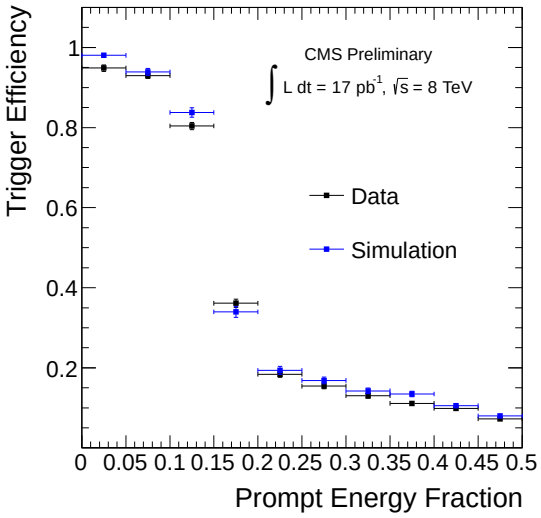


Figure 5.12: Single jet efficiency for jets with less than 15% prompt energy fraction as a function of offline prompt energy fraction.

needed as the statistical uncertainties on the individual ratio bins are larger due to limited statistics. We assign a correction of 97% and a conservative systematic uncertainty of 2% for each jet passing this filter based on the average and the spread of the fit results for $p_T$, $\eta$, and $\phi$. Similar performance of the filters described in Sections 5.9.2 and 5.9.3 is expected, since both filters act on similar sets of tracks.

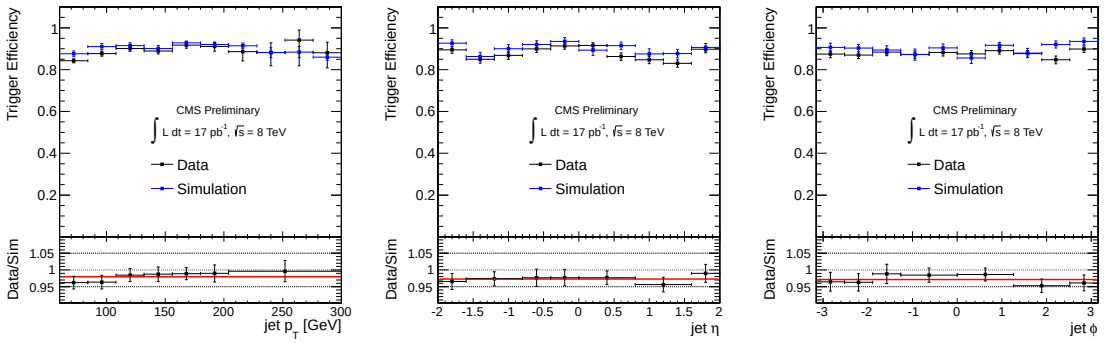


Figure 5.13: Single jet efficiency as a function of jet $p_T$, $\eta$ and $\phi$ for jets with maximally 15% prompt energy fraction.

### 5.9.4 Overall trigger efficiency

Each of the trigger filters has been analyzed individually by determining performance differences between data and simulation. Observable discrepancies are accounted for as corrections in Sections 5.9.2 and 5.9.3 and the uncertainties on the corrections are treated as systematic uncertainties. The trigger used in the physics analysis requires at least two jets passing the filters from Sections 5.9.2 and 5.9.3, hence corrections need to be applied twice, while systematic uncertainties need to be added as fully correlated. Additionally, systematic uncertainties related to filters from Sections 5.9.2 and 5.9.3 are both related to the reconstruction of prompt tracks. We therefore adopt a conservative approach and also assume that they are correlated. The systematic uncertainty assigned to the filter from Section 5.9.1 is related to the jet transverse energies, and therefore can be treated as uncorrelated. The total correction applied to the per-event trigger efficiency determined from simulation is thus 0.89 with a total relative systematic uncertainty of 6%.

## 5.10 Total signal efficiency systematic uncertainty

Table 5.5 summarizes the sources of systematic uncertainties on the signal efficiency. The various effects are assumed uncorrelated and therefore added in quadrature with a total uncertainty between 8–10% depending on the signal model.

Table 5.5: Summary of signal efficiency systematic uncertainties. *Applies only to samples with $H^0$ mass of 200 and 400 GeV.

| Source | Uncertainty |
|---|---|
| Trigger efficiency | 6% |
| Tracking efficiency | 4% |
| Jet energy scale | 3-5%(*) |
| Jet momentum bias | 1-5% |
| Pileup modelling | 2% |
| Total | 8-10% |

# Chapter 6

# Results

In this final chapter we present the signal reconstruction efficiencies for the Hidden Valley model as a function of the masses and lifetimes of the exotic $H^0$ and $X^0$ particles. We then unblind the data in the signal region and confront it with a signal hypothesis. The data is consistent with the background-only hypothesis, so we set upper limits that depend on the reconstruction efficiency of the signal models.

## 6.1 Long-lived particle reconstruction efficiency

In order to visualize the capabilities of the CMS detector for reconstructing long-lived particles decaying to dijets, the reconstructed dijet mass and $L_{xy}$ distributions for selected signal models are shown in Fig. 6.1. We assume the cross-section of the $H^0 \to 2X^0$ process to be 1 pb and the branching ratio to quarks ($X^0 \to q\overline{q}$) to be 100%.

The signal reconstruction efficiency is obtained by applying the final selection criteria (Section 4.2) to the dijet candidate that was chosen after candidate preselection and then counting the surviving events. The efficiency for all signal models considered in this analysis is presented in Table 6.1.

The signal reconstruction efficiency is examined further as a function of the various properties of the signal event. Fig. 6.2 presents the efficiency as a function of the $X^0$ particle's transverse displacement, Fig. 6.3 shows the efficiency as a function of the transverse impact

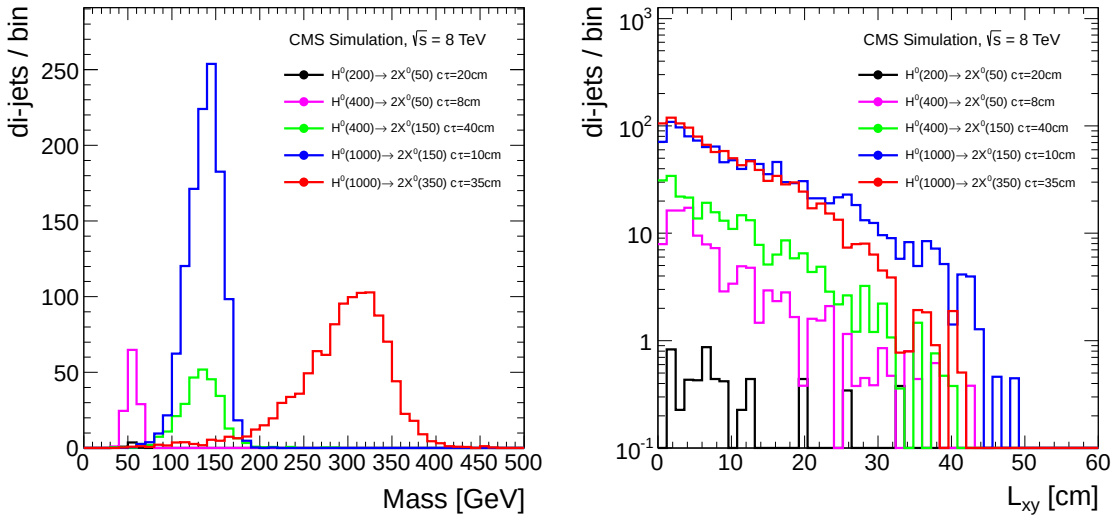


Figure 6.1: The reconstructed dijet mass and $L_{xy}$ for selected signal models; central lifetime out of the three available is presented.

Table 6.1: Signal reconstruction efficiency ($\epsilon$) for $\mathrm{H}^0 \to 2\mathrm{X}^0$ $\left(\mathrm{X}^0 \to q\bar{q}\right)$ in simulated signal models. The trigger and reconstruction efficiencies are both included in the efficiency. The uncertainties are statistical only.

| $\mathrm{H}^0$ [GeV] | $\mathrm{X}^0$ [GeV] | $c\tau$ [cm] | $\langle L_{xy} \rangle$ [cm] | $\epsilon$ [%] |
|---|---|---|---|---|
| 200 | 50 | 2 | 3 | $0.25 \pm 0.05$ |
| 200 | 50 | 20 | 30 | $0.15 \pm 0.04$ |
| 400 | 50 | 0.8 | 2.6 | $5.6 \pm 0.2$ |
| 400 | 50 | 8 | 26 | $3.3 \pm 0.2$ |
| 400 | 50 | 80 | 260 | $0.3 \pm 0.06$ |
| 400 | 150 | 4 | 3 | $15.6 \pm 0.4$ |
| 400 | 150 | 40 | 30 | $7.6 \pm 0.3$ |
| 400 | 150 | 400 | 300 | $0.6 \pm 0.1$ |
| 1000 | 150 | 1 | 2.5 | $41.3 \pm 0.5$ |
| 1000 | 150 | 10 | 25 | $31.1 \pm 0.5$ |
| 1000 | 150 | 100 | 250 | $4.8 \pm 0.2$ |
| 1000 | 350 | 3.5 | 2.9 | $49.2 \pm 0.5$ |
| 1000 | 350 | 35 | 29 | $30.9 \pm 0.5$ |
| 1000 | 350 | 350 | 290 | $4.4 \pm 0.2$ |

parameters of the $q\bar{q}$ system, while Fig. 6.4 presents the efficiency as a function of $H^0$ and $X^0$ transverse momenta.

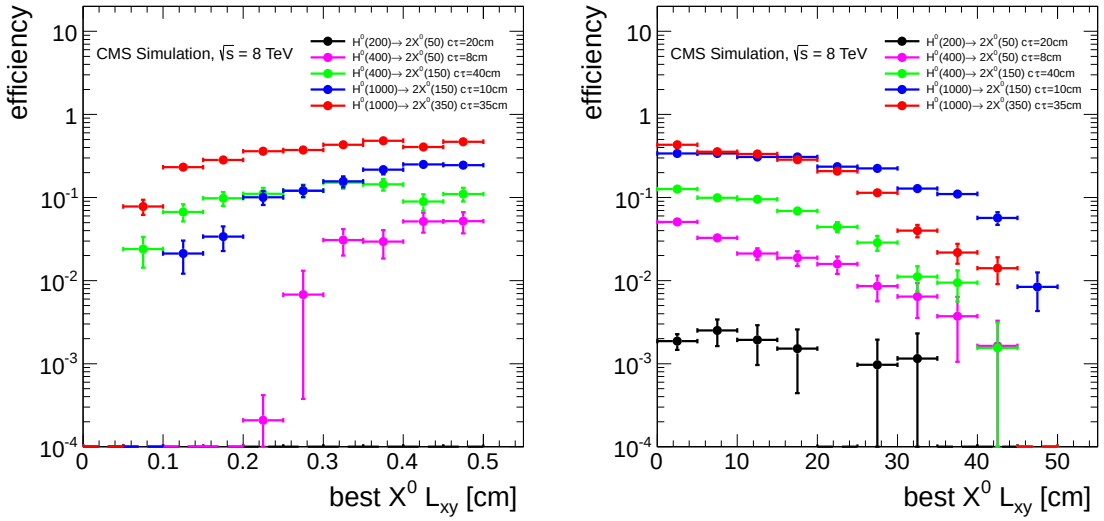


Figure 6.2: Signal reconstruction efficiency as a function of the $X^0$ transverse displacement ($L_{xy}$). The turn-on curve for small displacement is shown on the left, while the turn-off for large displacements is presented on the right.

## 6.2 Data in the signal region

Table 6.2 summarizes the observed event counts in the signal region for the optimized selections detailed in Section 4.2. The data is found to be in good agreement with the background-only hypothesis. In addition, the two selected events are examined using event displays and are found to be consistent with background events as described in the caption of Fig. 6.5.

Table 6.2: Observed events and predicted background for the optimized selections.

| **$L_{xy}$ selection** | **low** | **high** |
|---|---|---|
| **Predicted Background** | $1.60 \pm 0.58$(stat+sys) | $1.14 \pm 0.54$(stat+sys) |
| **Observed events** | 2 | 1 |

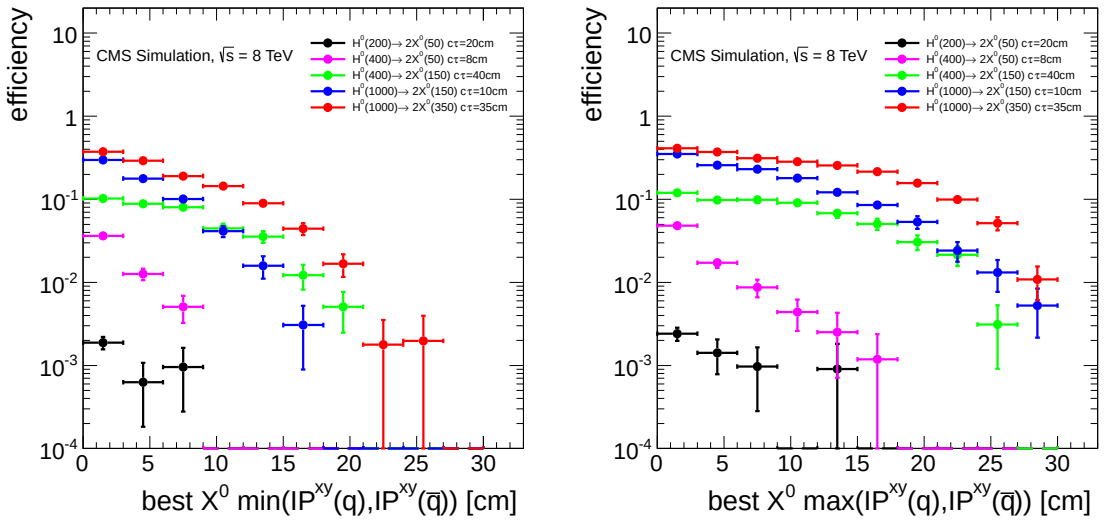


Figure 6.3: Signal reconstruction efficiency as a function of the transverse impact parameters of the $q\overline{q}$ system. The efficiency as a function of the smaller of the two $q\overline{q}$ transverse impact parameters is shown on the left, while the efficiency as a function of the larger one is presented on the right.

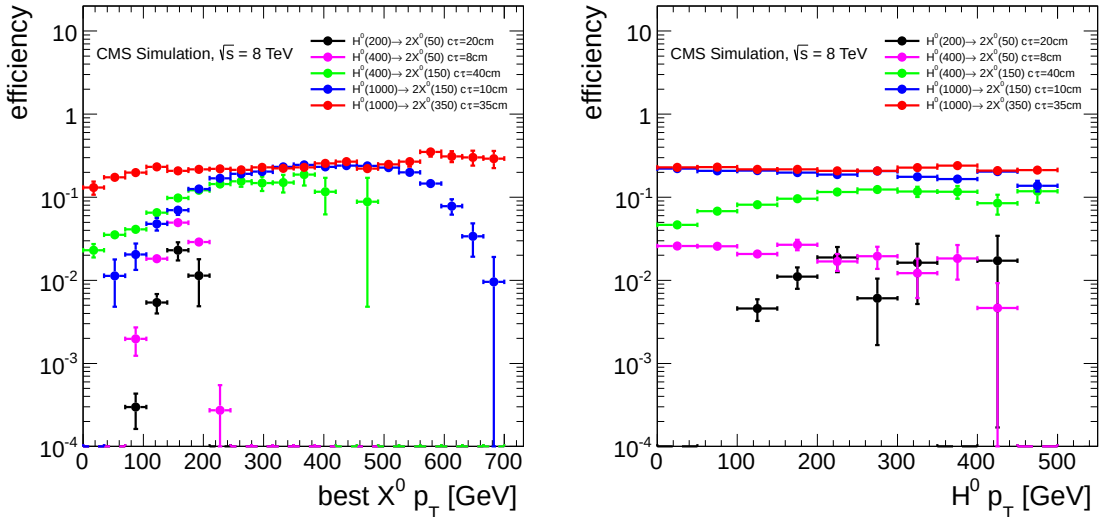


Figure 6.4: Signal reconstruction efficiency as a function of the $X^0$ particle transverse momentum (left) and as a function of the $H^0$ particle transverse momentum (right).

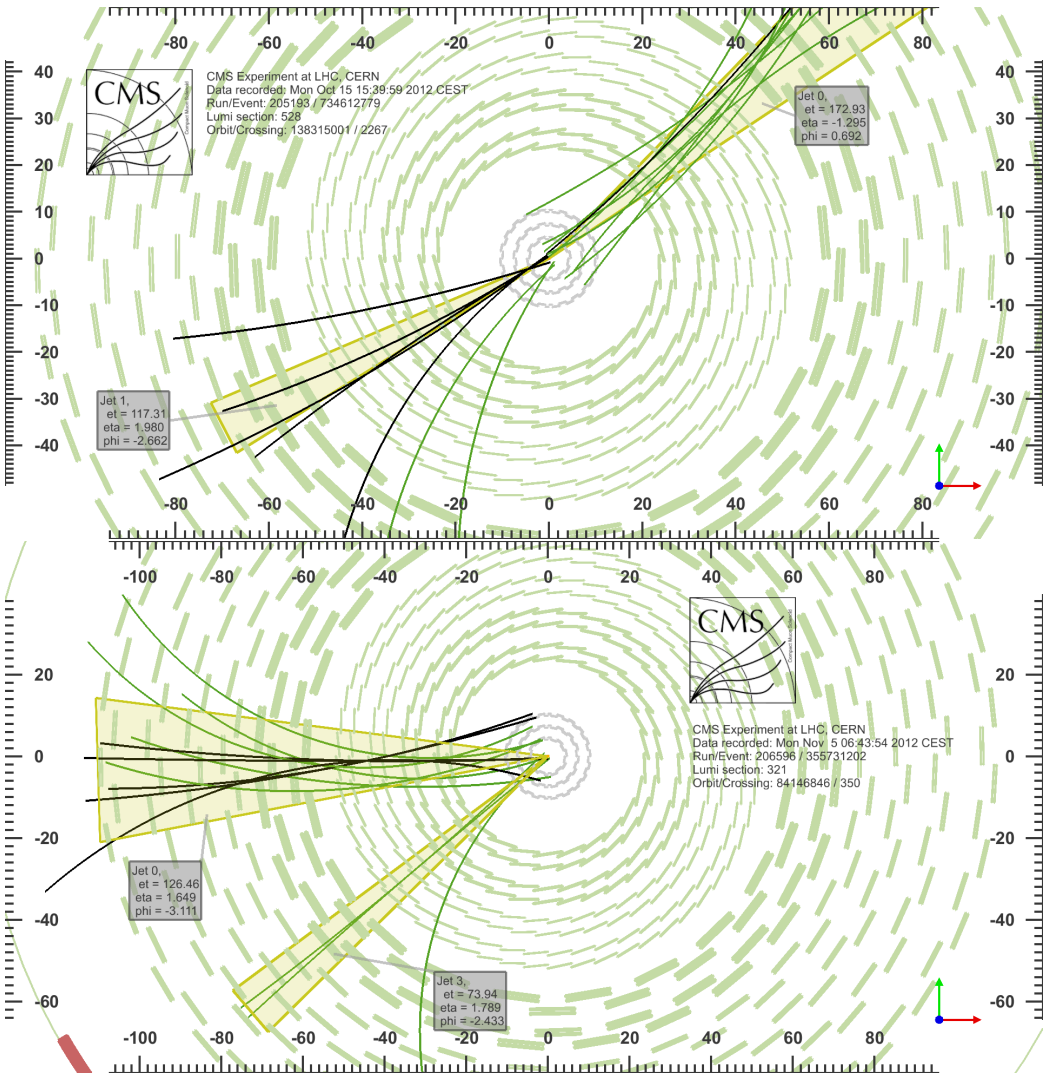


Figure 6.5: Event displays of the two events passing the optimized selection where only the selected jet pair (yellow cones) and the associated tracks (curved lines) are shown, other objects being removed. The tracks that fit the secondary vertex are colored black. Event 1 (top) with dijet invariant mass of 770 GeV, which passes only the *low* $L_{xy}$ selection, contains a secondary vertex, displaced transversely by 5 cm, containing five tracks from one jet and one track from the other. The 5-track vertex is consistent with a B meson vertex with an apparent invariant mass below 5 GeV. Event 2 (bottom) has a dijet invariant mass of 75 GeV, and passes both *low* and *high* $L_{xy}$ selections. It contains a secondary vertex displaced transversely by 44 cm, and contains five tracks, two of which are associated with both of the closely spaced jets. The vertex invariant mass is low and its position coincides with one of the silicon tracker layers, making it consistent with a nuclear interaction vertex.

## 6.3 Limits

We set 95% confidence level (CL) upper limits for a counting experiment using the $CL_s$ method [51, 52]. The limit calculation takes into account the systematic uncertainties described in Chapter 5 by introducing a nuisance parameter for each uncertainty, marginalised by a log-normal prior distribution.

As a first step, upper limits are placed on the mean number of events that could pass the selection requirements. The resulting observed upper limits are 4.6 events for the *low* $L_{xy}$ selection and 3.7 events for the *high* selection. These limits are independent of the particular model assumed for production of long-lived particles.

As a second step, an upper limit is quoted on the cross section for the production of $H^0 \to 2X^0$ times the branching fraction squared, $B^2$, for $X^0$ to decay into $q\overline{q}$. The observed and expected limits are shown in Fig. 6.6. In order to expand the number of tested models, the lifetime distributions of the signal MC events are reweighted to different mean values, namely $0.4\tau$, $0.6\tau$, and $1.4\tau$ for every lifetime $\tau$ and mass combination listed in Table 6.1. Event weights are computed as the product of weights assigned to each $X^0$ candidate in the event. The reweighted signal reconstruction efficiencies are then used to compute the expected and observed limits for these additional mean lifetime values.

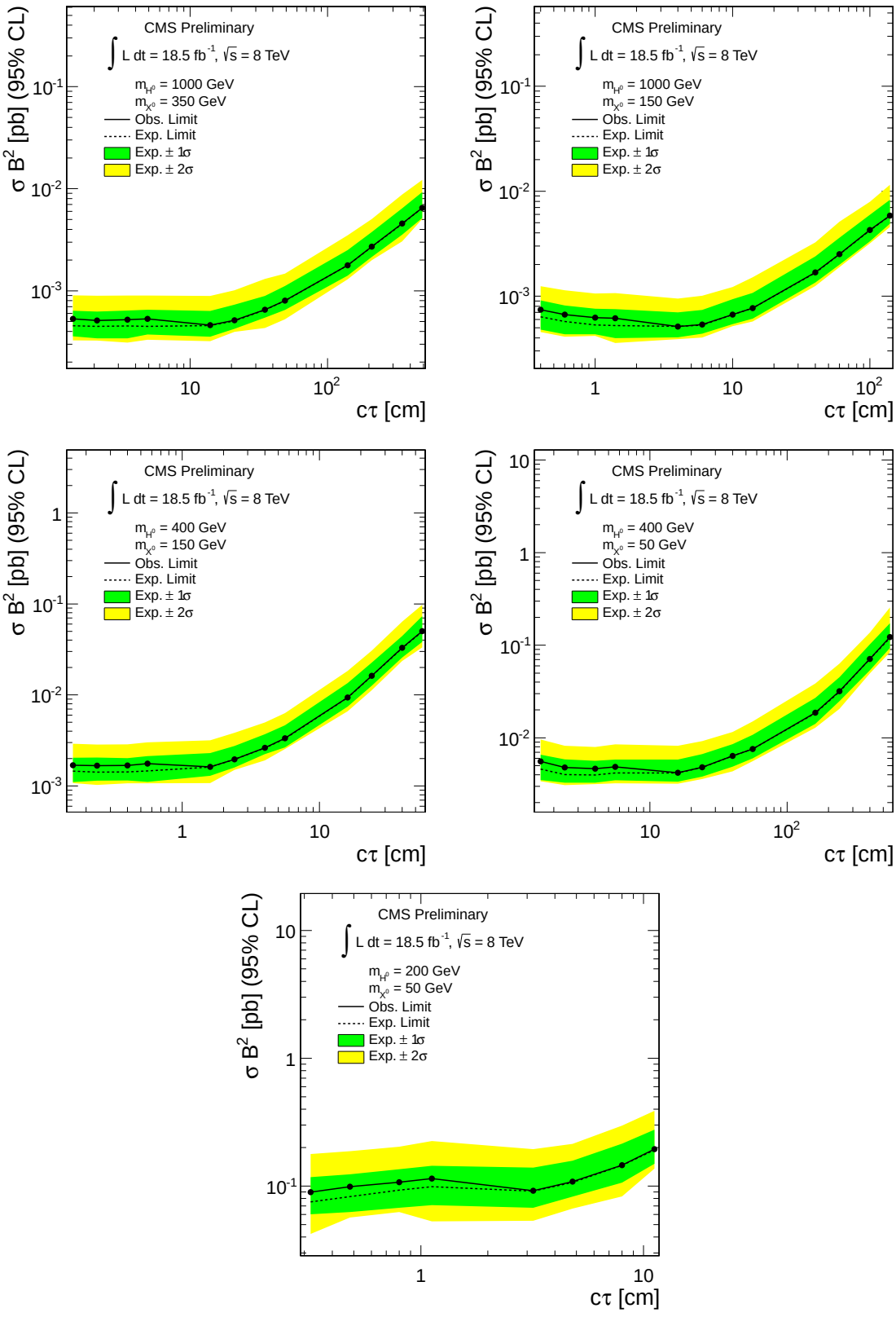


Figure 6.6: Expected and observed 95% CL limits for all tested signal models.

# Chapter 7

# Conclusions

Using data from the CMS detector at the LHC, a search for long-lived particles, $X^0$, produced in pp collisions at $\sqrt{s} = 8\,\text{TeV}$ and decaying to quark-antiquark pairs has been performed. For the first time a purely hadronic signature of long-lived particles has been explored at CMS. The observed results are consistent with SM expectations and are used to derive upper limits on the product of cross section times branching fraction for a scalar particle, $H^0$, in the mass range 200 to 1000 GeV, decaying into a pair of $X^0$ bosons in the mass range 50 to 350 GeV, each of which decays to quark-antiquark pairs. For $H^0$ masses of 400–1000 GeV, $X^0$ masses of 50–350 GeV, and $X^0$ lifetimes of $0.1 < c\tau < 200$ cm, the upper limits are typically 0.5–100 fb. For a $H^0$ mass of 200 GeV, the corresponding limits are in the range of 0.09–0.2 pb for $X^0$ lifetimes of $0.2 < c\tau < 10$ cm. These are the most stringent limits in this channel to date. In addition, the search allows for interpretation in terms of other models that predict the existence of massive long-lived particles with at least two hadronic jets among their decay products.

# Appendix A

# Hierarchical Clusters

In this analysis dijet tracks are clustered according to their $L_{xy}^{\text{exp}}$ values, as described in Section 3.2, using a method known as *hierarchical clustering*.

Hierarchical clustering connects elements of an unclustered set using a similarity (linkage) criterion, as shown schematically in Figure A.1.

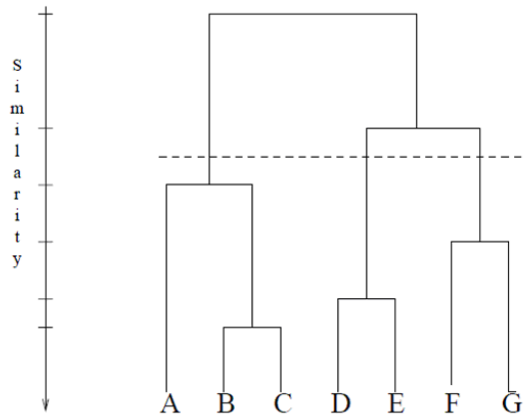


Figure A.1: Dendrogram presenting hierarchical clustering.

Initially each element is its own cluster (A-G). Each of the next steps merges the two most similar clusters into one. In the case of clustering numbers the similarity criterion is the smallest distance between clusters. For clusters A and B the similarity is obtained as

follows:

$$\min\{\, d(x,y) : x \in \mathcal{A},\, y \in \mathcal{B}\,\},\;\; d(x,y) = |x - y| \tag{A.1}$$

where $\mathcal{A}$ and $\mathcal{B}$ are already existing clusters. As presented in Figure A.1 the first step connects clusters B and C, the second step connects clusters D and E, etc. The procedure is repeated until the similarity criterion is no longer satisfied. In Figure A.1 the minimal similarity criterion is schematically presented as a horizontal dashed line. The clustering procedure results in two clusters: ABC and DEFG. In the dijet analysis we cluster tracks according to their $L_{xy}^{\rm exp}$ if the minimal distance between the clusters (Eqn. A.1) does not exceed 15% of the secondary vertex $L_{xy}$.

# Appendix B

# Impact of the signal efficiency systematic uncertainty on the expected limit

The impact of the signal efficiency systematic uncertainty on the expected limit is studied. The luminosity and background predictions together with their uncertainties are fixed to the ones used in this analysis, while the signal efficiency and its relative uncertainty are varied.

Figure B.1 shows the relative expected limit and $\pm 1\sigma$ band degradation as the systematic uncertainty on signal efficiency is varied from 0 to 90%. The degradation of the limit does not depend on the central value of the efficiency itself. Relative to a limit obtained with no uncertainty, a degradation of 10% is observed for a 30% systematic uncertainty. The limit degradation has also been studied assuming Gaussian or Log-normal parametrizations of the nuisance parameters yielding similar results.

In this analysis the systematic uncertainty on the signal efficiency has been conservatively estimated to be at most 10% for all signal models considered. A precise estimate of its value is of secondary importance, given a small impact on the resulting limit.

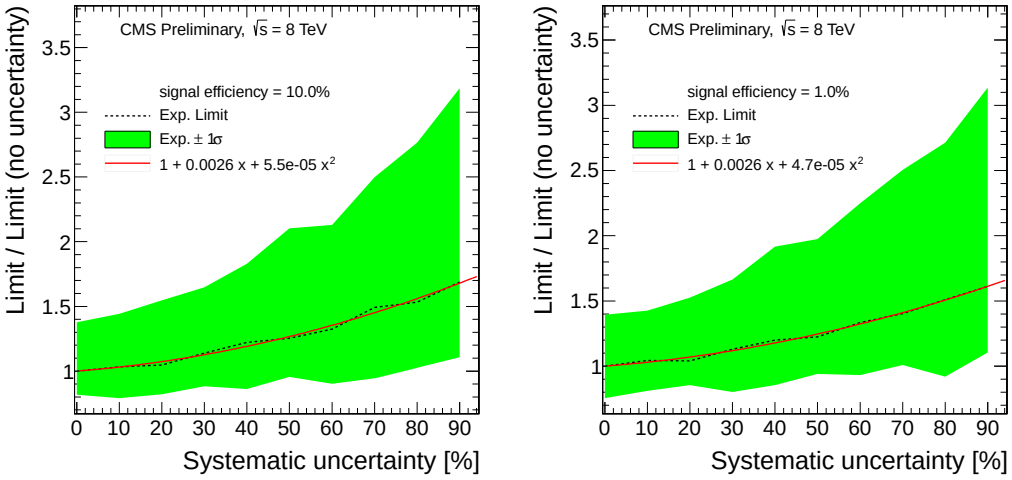


Figure B.1: Expected limit degradation as a function of signal efficiency systematic uncertainty. The signal efficiency central value is assumed to be 10% (left) and 1% (right). A second order polynomial is fitted to the expected limit graph with the fit parameter values listed in the legend.

# References


[1] S. Glashow, "Partial Symmetries of Weak Interactions," *Nucl.Phys.*, vol. 22, pp. 579–588, 1961.

[2] A. Salam, "Weak and Electromagnetic Interactions," *Conf.Proc.*, vol. C680519, pp. 367–377, 1968.

[3] C. G. Tully, *Elementary particle physics in a nutshell*. Princeton, NJ: Princeton Univ. Press, 2011.

[4] P. W. Anderson, "Plasmons, Gauge Invariance, and Mass," *Phys.Rev.*, vol. 130, pp. 439–442, 1963.

[5] F. Englert and R. Brout, "Broken Symmetry and the Mass of Gauge Vector Mesons," *Phys.Rev.Lett.*, vol. 13, pp. 321–323, 1964.

[6] P. W. Higgs, "Broken Symmetries and the Masses of Gauge Bosons," *Phys.Rev.Lett.*, vol. 13, pp. 508–509, 1964.

[7] M. Baak and R. Kogler, "The global electroweak Standard Model fit after the Higgs discovery," 2013.

[8] S. P. Martin, "A Supersymmetry primer," 1997.

[9] N. Arkani-Hamed, S. Dimopoulos, and G. Dvali, "The Hierarchy problem and new dimensions at a millimeter," *Phys.Lett.*, vol. B429, pp. 263–272, 1998.

[10] A. Zee, "Quantum field theory in a nutshell," 2003.

[11] H. Georgi and S. Glashow, "Unity of All Elementary Particle Forces," *Phys.Rev.Lett.*, vol. 32, pp. 438–441, 1974.

[12] A. Buras, J. Ellis, M. Gaillard, and D. Nanopoulos, "Aspects of the grand unification of strong, weak and electromagnetic interactions," *Nuclear Physics B*, vol. 135, no. 1, pp. 66 – 92, 1978.

[13] G. Bertone, D. Hooper, and J. Silk, "Particle dark matter: evidence, candidates and constraints," *Physics Reports*, vol. 405, no. 56, pp. 279 – 390, 2005.

[14] Y. Fukuda *et al.*, "Measurements of the solar neutrino flux from Super-Kamiokande's first 300 days," *Phys.Rev.Lett.*, vol. 81, pp. 1158–1162, 1998.

[15] D. Decamp *et al.*, "Determination of the Number of Light Neutrino Species," *Phys.Lett.*, vol. B231, p. 519, 1989.

[16] M. Fukugita and T. Yanagida, "Baryogenesis Without Grand Unification," *Phys.Lett.*, vol. B174, p. 45, 1986.

[17] V. Sahni and A. A. Starobinsky, "The Case for a positive cosmological Lambda term," *Int.J.Mod.Phys.*, vol. D9, pp. 373–444, 2000.

[18] S. Rugh and H. Zinkernagel, "The quantum vacuum and the cosmological constant problem," *Studies in History and Philosophy of Science Part B: Studies in History and Philosophy of Modern Physics*, vol. 33, no. 4, pp. 663 – 705, 2002.

[19] M. J. Strassler and K. M. Zurek, "Echoes of a hidden valley at hadron colliders," *Phys.Lett.*, vol. B651, pp. 374–379, 2007.

[20] M. J. Strassler, "Possible effects of a hidden valley on supersymmetric phenomenology," 2006.

[21] M. J. Strassler and K. M. Zurek, "Discovering the Higgs through highly-displaced vertices," *Phys. Lett. B*, vol. 661, p. 263, 2008.

[22] T. Han, Z. Si, K. M. Zurek, and M. J. Strassler, "Phenomenology of hidden valleys at hadron colliders," *JHEP*, vol. 07, p. 008, 2008.

[23] M. J. Strassler, "On the Phenomenology of Hidden Valleys with Heavy Flavor," 2008.

[24] J. L. Hewett, B. Lillie, M. Masip, and T. G. Rizzo, "Signatures of long-lived gluinos in split supersymmetry," *JHEP*, vol. 09, p. 070, 2004.

[25] R. Barbier, C. Berat, M. Besancon, M. Chemtob, A. Deandrea, *et al.*, "R-parity violating supersymmetry," *Phys. Rept.*, vol. 420, p. 1, 2005.

[26] L. Basso, A. Belyaev, S. Moretti, and C. H. Shepherd-Themistocleous, "Phenomenology of the minimal B-L extension of the Standard model: Z' and neutrinos," *Phys. Rev. D*, vol. 80, p. 055030, 2009.

[27] T. Aaltonen *et al.*, "Search for heavy metastable particles decaying to jet pairs in $p\bar{p}$ collisions at $\sqrt{s} = 1.96$ TeV," *Phys. Rev. D*, vol. 85, p. 012007, 2012.

[28] V. M. Abazov *et al.*, "Search for Resonant Pair Production of long-lived particles decaying to $b\bar{b}$ in $p\bar{p}$ collisions at $\sqrt{s} = 1.96$-TeV," *Phys. Rev. Lett.*, vol. 103, p. 071801, 2009.

[29] G. Aad *et al.*, "Search for a light Higgs boson decaying to long-lived weakly-interacting particles in proton-proton collisions at $\sqrt{s} = 7$ TeV with the ATLAS detector," *Phys.Rev.Lett.*, vol. 108, p. 251801, 2012.

[30] S. Chatrchyan *et al.*, "Search in leptonic channels for heavy resonances decaying to long-lived neutral particles," *JHEP*, vol. 1302, p. 085, 2013.

[31] "Search for long-lived neutral particles decaying to dijets," Tech. Rep. CMS-PAS-EXO-12-038, CERN, Geneva, 2013.

[32] L. Evans and P. Bryant, "LHC Machine," *JINST*, vol. 3, p. S08001, 2008.

[33] O. S. Bruning, P. Collier, P. Lebrun, S. Myers, R. Ostojic, *et al.*, "LHC Design Report. 1. The LHC Main Ring," 2004.

[34] R. Aaij *et al.*, "Absolute luminosity measurements with the LHCb detector at the LHC," *JINST*, vol. 7, p. P01010, 2012.

[35] S. Chatrchyan *et al.*, "The CMS experiment at the CERN LHC," *JINST*, vol. 03, p. S08004, 2008.

[36] R. Fruhwirth, "Application of Kalman filtering to track and vertex fitting," *Nucl.Instrum.Meth.*, vol. A262, pp. 444–450, 1987.

[37] V. Khachatryan *et al.*, "CMS Tracking Performance Results from Early LHC Operation," *Eur. Phys. J. C*, vol. 70, p. 1165, 2010.

[38] CMS Collaboration, "Particle–flow event reconstruction in CMS and performance for jets, taus, and $E_{\mathrm{T}}^{\mathrm{miss}}$," CMS Physics Analysis Summary CMS-PAS-PFT-09-001, CERN, 2009.

[39] CMS Collaboration, "Commissioning of the particle-flow event reconstruction with the first LHC collisions recorded in the CMS detector," CMS Physics Analysis Summary CMS-PAS-PFT-10-001, CERN, 2010.

[40] M. Cacciari, G. P. Salam, and G. Soyez, "The Anti-k(t) jet clustering algorithm," *JHEP*, vol. 04, p. 063, 2008.

[41] S. Cittolin, A. Rcz, and P. Sphicas, *CMS The TriDAS Project: Technical Design Report, Volume 2: Data Acquisition and High-Level Trigger. CMS trigger and data-acquisition project.* Technical Design Report CMS, Geneva: CERN, 2002.

[42] D. Bourilkov, R. C. Group, and M. R. Whalley, "LHAPDF: PDF use from the Tevatron to the LHC," 2006.

[43] T. Sjostrand, S. Mrenna, and P. Z. Skands, "PYTHIA 6.4 Physics and Manual," *JHEP*, vol. 0605, p. 026, 2006.

[44] S. Agostinelli *et al.*, "GEANT4: A simulation toolkit," *Nucl. Instrum. Meth. A*, vol. 506, p. 250, 2003.

[45] W. Waltenberger, "Adaptive vertex reconstruction," Tech. Rep. CMS-NOTE-2008-033, CERN, Geneva, Jul 2008.

[46] D. Giordano and G. Sguazzoni, "CMS reconstruction improvements for the tracking in large pile-up events," *J.Phys.Conf.Ser.*, vol. 396, p. 022044, 2012.

[47] CMS Collaboration, "CMS Luminosity Based on Pixel Cluster Counting - Summer 2013 Update," Tech. Rep. CMS-PAS-LUM-13-001, CERN, Geneva, 2013.

[48] Particle Data Group, J. Beringer, *et al.*, "Review of Particle Physics," *Phys. Rev. D*, vol. 86, p. 010001, 2012.

[49] V. Khachatryan *et al.*, "Strange Particle Production in pp Collisions at $\sqrt{s} = 0.9$ and 7 TeV," *JHEP*, vol. 05, p. 064, 2011.

[50] S. Chatrchyan *et al.*, "Determination of Jet Energy Calibration and Transverse Momentum Resolution in CMS," *JINST*, vol. 6, p. P11002, 2011.

[51] A. L. Read, "Presentation of search results: The CL(s) technique," *J. Phys. G*, vol. 28, p. 2693, 2002.

[52] T. Junk, "Confidence level computation for combining searches with small statistics," *Nucl. Instrum. Meth. A*, vol. 434, p. 435, 1999.